



HAL
open science

Identification and characterization of a non-canonical menaquinone-linked formate dehydrogenase

Rodrigo Arias-Cartin, Alexandre Uzel, Farida Seduk, Guillaume Gerbaud, Fabien Pierrel, Marianne Broc, Régine Lebrun, Bruno Guigliarelli, Axel Magalon, Stéphane Grimaldi, et al.

► To cite this version:

Rodrigo Arias-Cartin, Alexandre Uzel, Farida Seduk, Guillaume Gerbaud, Fabien Pierrel, et al.. Identification and characterization of a non-canonical menaquinone-linked formate dehydrogenase. *Journal of Biological Chemistry*, 2022, 298 (2), pp.101384. 10.1016/j.jbc.2021.101384 . hal-03431446

HAL Id: hal-03431446

<https://amu.hal.science/hal-03431446>

Submitted on 26 Nov 2021

HAL is a multi-disciplinary open access archive for the deposit and dissemination of scientific research documents, whether they are published or not. The documents may come from teaching and research institutions in France or abroad, or from public or private research centers.

L'archive ouverte pluridisciplinaire **HAL**, est destinée au dépôt et à la diffusion de documents scientifiques de niveau recherche, publiés ou non, émanant des établissements d'enseignement et de recherche français ou étrangers, des laboratoires publics ou privés.



Distributed under a Creative Commons Attribution 4.0 International License

Identification and characterization of a non-canonical menaquinone-linked Formate dehydrogenase

Running title: Formate dehydrogenases from *Bacillus subtilis*

Rodrigo Arias-Cartin^{1,2##†}, Alexandre Uzel^{2*}, Farida Seduk¹, Guillaume Gerbaud², Fabien Pierrel³, Marianne Broc¹, Régine Lebrun⁴, Bruno Guigliarelli², Axel Magalon¹, Stéphane Grimaldi^{2†} and Anne Walburger^{1†}

¹ Aix Marseille Université, CNRS, Laboratoire de Chimie Bactérienne (UMR7283), IMM, IM2B, 13009 Marseille, France.

² Aix Marseille Université, CNRS, Laboratoire de Bioénergétique et Ingénierie des Protéines (UMR7281), IMM, IM2B, 13009 Marseille, France.

³ Grenoble Alpes Université, CNRS, Grenoble INP, TIMC, 38000 Grenoble, France.

⁴ Aix Marseille Université, CNRS, Plateforme Protéomique de l'IMM, IM2B Marseille Protéomique (MaP), 13009 Marseille, France.

† To whom correspondence should be addressed. E-mail:

walburger@imm.cnrs.fr;

rodrigo.ariascartin@pasteur.fr;

stephane.grimaldi@univ-amu.fr

Present address: Stress Adaptation and Metabolism Unit, Department of Microbiology, Pasteur Institute, CNRS, Microbiologie Intégrative et Moléculaire (UMR 2001), Paris, France.

* These authors contributed equally to this work.

This article contains Figures S1–S7, Tables S1-S9 and supporting Ref. 75-89

Abstract:

The Mo/W-*bis*PGD Formate Dehydrogenases (FDHs) family interplays in several metabolic pathways ranging from carbon fixation to energy harvesting owing to their reaction with a wide variety of redox partners. Indeed, this metabolic plasticity is due to the diverse structure, cofactor content and substrates employed by partner subunits interacting with the catalytic hub. Here, we have unveiled two non-canonical FDHs in *Bacillus subtilis* which are organized into two-subunit complexes with unique features, ForCE1 and ForCE2. The ForC catalytic subunit interacts with an unprecedented partner subunit ForE and its amino acid sequence within the active site deviates from the consensus residues typically associated to FDH activity, with an histidine residue naturally substituted by a glutamine. The ForE essential subunit mediates the utilization of menaquinone as electron acceptor as shown by the formate:menadione oxidoreductase activity of both enzymes, their copurification with menaquinone and the distinctive detection of a protein-bound neutral menasemiquinone radical by multifrequency EPR experiments on the purified enzymes. Moreover, EPR characterization of both FDHs reveals the presence of several [Fe-S] clusters with distinct relaxation properties and a weakly anisotropic Mo(V) EPR signature consistent with the characteristic Mo-*bis*PGD cofactor of this enzyme family. Altogether, this work enlarges our representation of the FDH family by deciphering a non-canonical FDH, which differs both in terms of architecture, amino acid conservation around the Mo cofactor and reactivity.

Keywords:

bioenergetics, electron paramagnetic resonance (EPR), metalloenzyme, quinone, bacterial metabolism

Introduction

Formate dehydrogenases catalyze the oxidation of formate into CO₂ but have also been shown to catalyze the reverse reaction in methanogenic and/or acetogenic microorganisms, namely the reduction of CO₂ into formate (1). Metal-dependent FDHs (hereafter named FDHs) are exclusively found in prokaryotes and 3D-structure based phylogeny demonstrates that such enzymes were already present in the last universal common ancestor (LUCA) (2). In addition, paleogeochemistry suggests that in ancient times, compounds such as CO₂ and CH₄ were very abundant and that iron, molybdenum and tungsten were available and in soluble forms (3, 4). Indeed, FDHs harbor molybdenum or tungsten at the active site as well as one to five iron-sulfur cluster(s) (1, 5–8). The molybdenum or tungsten atom is coordinated by the dithiolene sulfurs of two organic *bis*pyranopterin guanosine dinucleotides (Mo/W-*bis*PGD) (1, 9), a cysteine or a selenocysteine and a sulfido group, all being essential for the activity (10–12). In addition, an histidine and an arginine residue located in proximity to the Mo atom (13) are strictly conserved in all FDHs described so far (Fig. 1A) and required for activity (14). These residues have been proposed to be involved in correct orientation or stabilization of the formate in the active site (15–17), but their role in activity is still debated. They could also act as a switch to obstruct alternatively the substrate and the product tunnels during catalysis, as suggested by the 3D-structure of the FDHs from *Rhodobacter capsulatus*, *Desulfovibrio vulgaris* Hildenborough and of the formyl-methanofuran dehydrogenase from *Methanothermobacter wolfeii* (18–20). Altogether, there is still a need for clarifying the exact role of these conserved residues surrounding the catalytic site in FDH activity.

From a physiological point of view, FDHs are involved in a wide range of anaerobic metabolic pathways, such as energy harvesting and carbon fixation (6, 9). This is due to the interaction of the catalytic subunit which harbors the Mo/W-*bis*PGD cofactor with partner subunits with the greatest diversity amongst the Mo/W-*bis* PGD enzymes superfamily (9). In methanogenic archaea, FDH is part of a complex that facilitate a two-step reduction of CO₂ to formate and then to formyl-methanofuran (20). In bacteria, the membrane bound FdnGHI complex couple formate oxidation to quinols production in anaerobic respiratory chains (21) and the soluble FdsABG from *Cupriavidus necator* and *Rhodobacter capsulatus* couple formate oxidation to NADH reduction that feed the reductive pentose phosphate cycle (22, 23). To summarize, FDHs are a group of heterogenous enzymes that display different subunits composition from the single monomeric subunit FdhF from *Escherichia coli* to the six-subunits complex formyl-methanofuran dehydrogenase (13, 20) and partner subunits hold a variety of redox cofactors ([Fe-S] clusters, hemes, F₄₂₀, FMN) that allow reaction with a wide variety of physiological redox partners, such as cytochromes, ferredoxins, NAD and quinones (1, 5–8). Altogether, identification and characterization of FDHs with variations in the amino acids surrounding the catalytic site or new subunit composition could improve our understanding of catalysis and expand the metabolic pathway repertory in which FDHs are participating.

In the archetypal gram-positive bacterium, *Bacillus subtilis*, an FDH activity has been detected in cells grown aerobically in rich medium (24). This is intriguing as FDHs are usually part of anaerobic metabolic pathways and *B.*

subtilis is not able to produce formate (25). These observations prompted us to search for the enzyme(s) involved in this activity. Combining bioinformatics with biochemistry, enzymology and EPR spectroscopy, we have identified and characterized two atypical FDH enzymes in *B. subtilis* and members of a new subfamily of FDHs. Notably, formate oxidation activity is measured while the conserved His residue in the active site is naturally substituted by a Gln. Moreover, both FDHs display a new architecture in which their catalytic subunit is associated with an unprecedented partner subunit that allows reactivity with menaquinone.

Results

The YjgC and YrhE sequences from B. subtilis encode putative metal-dependent FDHs

Scrutiny of the *B. subtilis* 168 genome indicates that it encodes for *yjgC* and *yrhE*, genes, whose ~110 kDa predicted proteins are paralogous with 61% of identity. Both putative oxidoreductases contain a C-terminal domain typical for Mo/W-bisPGD enzymes and characterized by motifs allowing the coordination of one Mo/W-bisPGD cofactor and one [4Fe-4S] cluster (Fig. S1A). Furthermore, both sequences contain a N-terminal extension with binding motifs for three [4Fe-4S] and one [2Fe-2S] clusters as determined by similarities (Fig. S1A). In particular, this region shares homologies with the N-terminal domain of the NuoG subunit of the NADH:ubiquinone oxidoreductase (i.e. complex I) and the catalytic subunit of NAD-dependent [NiFe]-hydrogenases (19, 26, 27). Such domain organization is also shared with other FDHs, notably FdsA from *C. necator* and *R. capsulatus* (Fig. S1B and S2A). A close-up alignment of the active site residues with previously characterized FDH sequences and YjgC and YrhE sequences is shown in Figure 1A. Whereas the typical metal Cys ligand and the strictly conserved Arg residue are present, the highly conserved His residue is substituted by a Gln in YjgC and YrhE. Phylogenetic analysis identified a large group of YjgC/YrhE-related sequences with the similar substitution in several bacterial and archaeal phyla, which are distinct from FdsA-related sequences (Fig. S2A). The presence of the Gln next to this Cys essential residue in the primary sequence questions the activity of these enzymes as FDHs. However, for the evidence that *B. subtilis* possesses at least one FDH is the existence of a putative *fdhD* gene encoding a sulfurtransferase crucial for FDH activity (12). In the *B. subtilis* genome, the *fdhD* gene is distant from the *yjgC* and *yrhE* loci (53' versus 18' and 39', respectively). Interestingly, the *yjgC* gene is predicted to be organized in operon with *yjgD* as *yjgC* and *yjgD* are co-expressed with a positive correlation of 0.98 (28, 29). The same holds true for the gene *yrhE* predicted to be in operon with *yrhD* as both are adjacent and co-expressed with a positive correlation of 0.99 (Fig. 1B). The *yjgD* and *yrhD* genes encode 21 kDa and 17 kDa polypeptides, with weak sequence overall identity (20%), and contain a DUF1641 domain of 38 amino acids of unknown function (PFAM PF07849). While YjgC/YrhE are related to FdsA, as illustrated by the YjgC structural model based on the 3D-structure of *R. capsulatus* FdsA (Fig. 1C) and the phylogenetic analysis (Fig. 1A and S1), YjgD and YrhD are distinct from FdsD or any of the other partner subunits previously characterized for a FDH, the complex I and [Ni-Fe] hydrogenases (6). In addition, YjgD and YrhD are predicted to be cofactor-less and have a distinct

sequence from the FdsC/FdhD sulfurtransferase or any specific chaperone involved in Mo-bisPGD maturation (30, 31). Altogether, these *in silico* analyses suggest that YjgC and YrhE are the enzymes involved in the FDH activity previously detected in *B. subtilis* (24) and question the role of YjgD and YrhD.

The YjgCD and YrhED are protein complexes with formate oxidizing activity

To test the activity of YjgC and YrhE as FDHs and the importance of YjgD and YrhD, the corresponding proteins were purified. First the *yjgCD* and *yrhED* operons were expressed in *B. subtilis* under the control of an inducible promoter and a 6-histidine tag was added at the N-terminus of the YjgC and YrhE proteins. Affinity purification of these proteins showed that YjgC and YrhE copurified with YjgD and YrhD, respectively, as identified by SDS-PAGE and mass spectrometry analysis (Fig. 2A, Tables S2 and S4). Mass spectrometry data are available via ProteomeXchange with identifier PXD028742. These results suggest that the proteins YjgD and YrhD interact physically with YjgC and YrhE, respectively. A full steady-state enzyme kinetic analysis of formate oxidation by YjgCD and YrhED using benzyl viologen as artificial electron acceptor is shown in Figure 2B. Using the Michaelis-Menten plot, a k_{cat} of 96 s^{-1} was measured for the YjgCD heterodimer (MW = 132 kDa) and a k_{cat} of 56 s^{-1} for the YrhED heterodimer (MW = 125 kDa) (Table 1). Both values are in the same range as the ones determined for FdsABG of *R. capsulatus* (36 s^{-1}) and *C. necator* (201 s^{-1}) (22, 26). Apparent $K_{\text{M}}^{\text{formate}}$ of 5 mM for YjgCD and 1 mM for YrhED are larger than the values of 0.281 mM and 0.31 mM determined for FdsABG of *R. capsulatus* and *C. necator*, respectively. As observed for other FDHs (22, 32, 33), both enzyme preparations exhibit a basic pH optimum, pH 10 for the YjgCD complex and pH 8.5 for YrhED (Fig. 2C). In conclusion, the YjgCD and YrhED are protein complexes with formate oxidizing activity with kinetic parameters comparable to other FDHs despite the fact that the amino acid sequence within the active site deviates from the consensus residues typically associated to FDH activity. Henceforth, the YjgC subunit was renamed ForC for Formate oxidorereductase Catalytic subunit and the YjgD subunit ForE for Formate oxidorereductase Essential subunit for reasons that will be presented at the end of the results section. As *B. subtilis* encodes two FDHs, YjgCD was renamed ForCE1 and YrhED ForCE2.

EPR analysis of ForCE1 and ForCE2

In order to characterize the cofactor content of the two enzymes, we next examined the EPR properties of purified ForCE1 and ForCE2 enzymes, either in their air-oxidized state or after incubation with a large excess of sodium formate or sodium dithionite. When measured in the [50-70 K] temperature range, the air-oxidized enzymes mainly display two essentially isotropic and partially overlapping EPR signals originating from two slow-relaxing $S = \frac{1}{2}$ species with g-values centered at 2.004 and 1.993. Their relative intensities are different in the two enzymes (Fig. 3A, traces 1 & 2). In a first step, the $g = 1.993$ signal which exhibits a partially resolved structure in both enzymes was investigated in detail. Optimally detected in the air-oxidized ForCE2 sample, this signal was further characterized by performing echo-detected field-swept experiments at W-band ($\sim 94 \text{ GHz}$) or continuous wave EPR measurements

at Q-band (~ 34 GHz) (Fig. 3B, inset and trace 2). At both frequencies, the $g = 1.993$ signal is well isolated and displays a rhombic shape well reproduced by considering a single species with g -values $g_{1,2,3} = 1.9971, 1.9933, 1.9890$. Whereas this model is unable to account for the resolved structure on the X-band EPR spectrum, addition of a strongly coupled proton with nearly isotropic ^1H hyperfine coupling tensor having principal values $A_{1,2,3} = 13, 13, 11$ MHz allows to reproduce the observed splittings (Fig. 3B, trace 1). Eventually, the multi-frequency EPR spectra are well simulated using the same set of g - and A -tensors as given above (Fig. 3B). The signal-giving species displays g -values fully consistent with those of a $4d^1$ Mo(V) ion with *bis*-pterin coordination (34). Notably, the corresponding g -tensor anisotropy ($g_1 - g_3 \sim 0.008$) is unusually low and most closely resembles that of the slow-type Mo(V) signal *Desulfovibrio alaskensis* NCIMB 13491 FDH ($g_1 - g_3 \sim 0.012$) (35). Moreover, the Mo(V) g -values in ForCE2 belong clearly to the correlation found for the variations of the g -tensor of Mo(V) species with a six-sulfur coordination (9, 34, 36) (Fig. S3). Finally, the magnitude of the proton hyperfine coupling tensor is comparable to that resolved on the Mo(V) EPR signal detected in *C. necator* FDH and assigned to a molybdenum-SH group (26). Therefore, the $g = 1.993$ signal similarly detected in ForCE1 and ForCE2 is unambiguously assigned to a Mo(V) species generated at their active site.

Interestingly, incubation of the enzymes with a large excess of sodium formate leads to an increase of the $g = 2.004$ signal relative to that of the Mo(V) species (Fig. 3A, traces 3 & 4). In addition, an axial signal with g -values 2.020 and 1.939 is detected in the ForCE1 spectrum measured at 50 K (Fig. 3A, trace 3). These observations are explained by partial reduction of the enzymes by sodium formate, and are consistent with the fact that the latter is the physiological substrate. The same axial signal is observed on the EPR spectrum of the dithionite-reduced samples of ForCE1 and ForCE2 measured at 100 K whereas the Mo(V) signal and the $g = 2.004$ species are no longer detected, consistent with further reduction of the latter and of the Mo(V) into the EPR-silent Mo(IV) state in these samples (Fig. 3C, traces 1 & 2). The slow relaxation properties of this axial signal and its g -values are typical for $S = \frac{1}{2}$ $[\text{2Fe-2S}]^{1+}$ clusters (37) and very similar to those detected in related FDHs from *Clostridium thermoaceticum*, *M. trichosporum* or *C. necator* (26, 38–40). Upon lowering the temperature to 50 K, new signals are detected peaking at $g = 2.047$ and 1.897 in ForCE1 (Fig. 3C, trace 3), and $g = 2.030$ and 1.912 in ForCE2 (Fig. 3C, trace 4). These are tentatively assigned to the g_1 and g_3 values of an additional slow relaxing $S = \frac{1}{2}$ $[\text{4Fe-4S}]^{1+}$ cluster. The corresponding intermediate g_2 value is estimated by numerical simulations (shown as red solid lines in Fig. 3C, traces 3 & 4), yielding to $g_{1,2,3} = 2.047, 1.948, 1.897$ and $2.030, 1.940, 1.912$ for this cluster in ForCE1 and ForCE2, respectively. Further lowering the temperature to 15 K leads to the appearance of additional overlapping signals peaking at 1.99 and 1.96 which most likely arise from an additional fast relaxing $[\text{4Fe-4S}]^{1+}$ center (Fig. 3C, traces 5 & 6). Being the sole EPR active center detected at 100 K, the $[\text{2Fe-2S}]$ cluster was used as an internal reference for spin quantitation measurements. Double integration of the EPR spectrum of a dithionite reduced ForCE1 sample buffered at pH 7.5 and measured at 15 K in non-saturating conditions (i.e. 0.1 mW) indicated that the detected signals

contribute to about 4.7 ± 0.4 spins/ ForCE1, assuming one [2Fe-2S] center per enzyme.

Overall, the present EPR analysis allows to identify the signature of several metal centers in ForCE1 and ForCE2, including that of their Moco, a [2Fe-2S] cluster and at least two other [4Fe-4S] centers with distinct relaxation properties. Importantly, the detected species have quite similar EPR signatures in both enzymes in agreement with the high identity percentage between ForC1 and ForC2 subunits.

A menasemiquinone radical stabilized within ForCE1 and ForCE2

An unexpected outcome of the EPR analysis presented above is the detection of an intense isotropic radical signal at $g = 2.004$ in ForCE1 and ForCE2 after incubation with sodium formate (Fig. 3A, traces 3 & 4). The radical peak-to-peak linewidth (~ 0.88 mT) is similar to that typically observed for protein-bound isoprenoid quinones (41, 42). To further identify its origin, its redox properties were investigated using EPR-monitored redox titration experiments performed on purified ForCE1 buffered at pH 6.0 and 7.5. The EPR amplitude of the radical measured against ambient redox potential changes according to a bell shape curve as expected for quinone species undergoing two successive one-electron reduction steps between the fully oxidized quinone and the fully reduced quinol state with an EPR-active semiquinone intermediate (Fig. 4A) (42–46). When the data were fitted using theoretical curves based on Eq. 1, midpoint potential values (E_1, E_2) = (-42 mV, -90 mV) and (-136, -175 mV) were obtained at pH 6 and 7.5, yielding to two-electron midpoint potential values E_m of -66 mV and -156 mV, respectively. Such values are consistent with those of low-potential menaquinones ($E_{m, \text{pH } 7.5} \text{ MK/MKH}_2 = -100 \pm 10$ mV) (47) such as MK-7, the major quinone present in *B. subtilis* membranes (48). The -60 mV/pH unit dependence of E_m in the investigated pH range indicates a $2\text{H}^+/2\text{e}^-$ reaction as measured for semiquinone radicals stabilized in exchangeable Q sites (43–45). In addition, the similar -60 mV/pH unit dependence of both E_1 and E_2 indicates that the neutral menasemiquinone (MSK) form (i.e. MSKH^*) is stabilized in this pH range. The maximum concentration of the radical was estimated to be 0.5 MSK/ForCE1 from double integration of its EPR spectrum measured under non-saturating conditions and using the [2Fe-2S] cluster as internal standard, assuming one [2Fe-2S]/enzyme.

The chemical nature of the radical was further confirmed by performing EPR experiments at higher microwave frequencies, as large unresolved hyperfine couplings typically obscure the g anisotropy of radicals measured at standard X-band frequencies (9-10 GHz) (49). Whereas the g tensor anisotropy of the radical in ForCE1 is only partially resolved at Q-band (~ 34 GHz), its g_3 component is clearly resolved at W-band (~ 94 GHz), the overall line shape remaining predominantly axial (Fig. 4B). Such features are again expected for protein-bound isoprenoid semiquinones (42, 50). In addition, EPR spectra recorded at X-, Q- and W-bands are well simulated using the same rhombic g -tensor with principal values $g_{1,2,3} = 2.0054, 2.0051, 2.0023$. These are very close to those measured for other protein-bound MSK such as in the Q_D site of *Escherichia coli* nitrate reductase (42, 46) (Fig. S6) or in the Q_A site of Zn-

substituted reaction center from *Blastochloris viridis* (41). Therefore, the EPR signal of the radical detected in ForCE1 can be assigned to a neutral MSK radical bound to the enzyme based on its EPR properties evaluated at several microwave frequencies as well as on its redox characteristics. This assignment also holds for the radical species detected in ForCE2, which exhibits similar g-values, as concluded from the comparative analysis of the W-band EPR spectra of the radical measured in ForCE1 and in ForCE2 (Fig. S6).

In addition, our data reveal that the detected MSK is highly stabilized in ForCE1 in the pH range from 6.0 to 7.5. The magnitude of the MSK stability constant is virtually independent of pH ($K_{S, \text{pH} = 6.0} \sim 7$, $K_{S, \text{pH} = 7.5} \sim 5$) and much larger than that expected for the unbound species, i.e. $K_{S, \text{free}} \sim 10^{-15}$. Hence, the calculated occupancy level R_{occ} of the ForCE1 Q-site which corresponds to the fraction of the site occupied by either MK, MSK or MKH₂ (irrespective of their protonation state) is close to unity at both pH values ($R_{\text{occ}} \sim 0.8$ at pH = 6.0 and ~ 0.9 at pH 7.5).

We confirmed the nature of the MK bound in purified ForCE1 and ForCE2 by analyzing lipid extracts with high-performance liquid chromatography coupled to electrochemical detection and mass spectrometry (HPLC-ECD-MS) (Fig. 4C). Lipid extracts from ForCE1 and ForCE2 show a predominant peak at 9.8 min, which coincides with the MK-7 standard. Mass spectrometry confirmed the identity of MK-7 (Fig. S5A). A minor peak of MK-8 was also detected (Fig. 4C), as supported by MS analysis (Fig. S5B). While the ForCE1:MK-7 ratio inferred by HPLC-ECD analysis shows a stoichiometric value of (1:0.87), the ForCE2:MK-7 ratio is above 1:1 stoichiometry (1:1.63) (Table S5). Nevertheless, the ForCE1:MK-7 ratio is in agreement with the amount of one MK-7 per complex quantified by EPR analysis.

ForCE1 and ForCE2 reduce MK-7 analogues

Having demonstrated that ForCE1 and ForCE2 enzymes are able to stabilize a MSK radical, we hypothesized that MK-7 is the electron acceptor during formate oxidation in *B. subtilis*. The enzymatic activity of purified ForCE1 and ForCE2 were analyzed in the presence of formate and menadione, a structural analogue of MK-7. Full steady-state enzyme kinetic analyses are shown in Figures 4D and 4E. To model experimental data, we used a Michaelis-Menten plot and found similar apparent low $K_{\text{M}}^{\text{menadione}}$ values for both enzymes (25 μM for ForCE1 and 23 μM for ForCE2) and a k_{cat} of 16.5 and 26.4 s^{-1} for ForCE1 and ForCE2, respectively (Table 1). The pH dependence of the formate:menadione oxidoreductase activity was determined and showed a pH optimum at ≈ 9 for both enzymes (Fig. 4F and S4). Altogether, our *in vitro* kinetic analyses show that ForCE1 and ForCE2 are able to couple formate oxidation to menadione reduction and we propose that MK-7 is the physiological electron acceptor during formate oxidation.

ForE1 is an essential subunit for Formate oxidoreductase activity of ForC1

To assess the importance of ForE1 or ForE2 in FDH activity, the *yjgC* (*forC1*) and *yrhE* (*forC2*) genes were expressed under the control of an inducible promoter in absence of *yjgD* (*forE1*) and *yrhD* (*forE2*), respectively. Despite many attempts, we were unable to purify the ForC2 subunit His-tagged in C-

terminal when produced without ForE2. On the contrary, we were able to purify ForC1 His-tagged in C-terminal (Fig. 2A, Table S3). This protein was able to oxidize formate with benzyl viologen (BV) as an artificial electron acceptor but at a residual $k_{\text{cat}} = 2 \text{ s}^{-1}$ compared to 96 s^{-1} for the ForCE1 complex (Table 1). HPLC-ECD analysis of ForC1 showed that very low quantities of MK-7 are associated with ForC1, as compared to ForCE1 (Fig. 4C, Table S5) and ForC1 is devoid of formate:menadione oxidoreductase activity (Table 1). Thus, the ForE1 subunit is required for formate:menadione oxidoreductase activity of ForC1 and most likely for MK-7 binding. Altogether, these results demonstrate the essential role of ForE1 in ForCE1 activity.

Discussion

FDHs have been widely studied as they reversibly catalyze formate oxidation into CO₂, CO₂ reduction being of high biotechnological interest. In contrast to other members of the Mo/W-*bis*PGD enzyme superfamily, FDHs exhibit a plethora of quaternary structure, subunit and redox center composition and of cellular localization allowing their integration in several anaerobic metabolic pathways as reviewed in (5, 7–9, 51). Here, we report on the identification, isolation and characterization of two atypical FDHs, ForCE1 and ForCE2, in the aerobic soil bacterium, *B. subtilis*. In contrast with other characterized FDHs, ForCEs (i) have a unique subunit composition, (ii) display modification of the hitherto conserved amino acid residues surrounding the metal active site and (iii) bind MK-7 while being cytosolic enzymes as shown by the homologous expression system reported here. Notably, ForCE1 and ForCE2 have each a Mo-*bis*PGD cofactor and bear up to 5 [Fe-S] clusters as determined by EPR spectroscopy. Additionally, both enzymes are able to perform formate:menadione oxidoreduction and have the ability to strongly bind MK-7 as indicated by HPLC-ECD-MS analysis and leads to the detection of an isotropic radical signal by EPR spectroscopy, assigned to a menasemiquinone signal.

Multimeric FDHs work in concert with other subunits to oxidize formate or to receive electrons from a donor in order to reduce CO₂. In other terms, partner subunits allow FDH integration into a specific metabolic pathway. Gene(s) encoding partner subunit(s) are organized into operons with the gene encoding the catalytic subunit. In FDHs from *B. subtilis*, genes encoding catalytic and partner subunits are organized into *forCE1* and *forCE2* operons. Our results have shown that purified ForC1 produced in absence of ForE1, binds weakly MK-7 and that it has lost formate:menadione oxidoreductase activity. Accordingly, we suggest that ForE is the partner subunit that allows to couple formate oxidation to quinone reduction. Such reaction has been demonstrated for the respiratory FdnGHI complex exemplified in *E. coli* (21). However, the partners subunits FdnHI are very distinct from ForE at the sequence level. The Mo-*bis*PGD containing FdnG subunit is the formate oxidation site connected through a 5 [Fe-S] clusters electron wire (in FdnGH) to the quinone reduction site in the transmembrane cytochrome FdnI. In contrast, the ForC subunit harbors the Mo-*bis*PGD cofactor formate oxidation site as well as 5 [Fe-S] clusters in the same polypeptide and the menaquinone reduction site hypothetically located at the ForCE interface (see discussion below). It must be noted that ForCE sequences are not predicted to contain any transmembrane segment neither hemes, as confirmed by EPR analysis of ForCE1 and ForCE2. Therefore, we conclude that the way the formate:menaquinone oxidoreduction occurs into ForCEs is unprecedented.

The ForC catalytic subunit presents high sequence similarity with FdsA from *R. capsulatus* and *C. necator* (Fig. S1) and a ForC1 structural model using the former has been built (Fig. 1C). In this model, electrons are logically shuttled from the Mo-*bis*PGD catalytic site along the [Fe-S] clusters (C1 to C4/C5) to the physiological electron acceptor. We hypothesize that MK-7 binds to the N-terminal region of ForC1 in such a way that the distance between the MK-7 and one of the two most N-terminus [Fe-S] clusters, namely: the [4Fe-4S]

(C4) or the [2Fe-2S] (C5) cluster (Fig. 1C) is compatible with physiological electron transfer (52). It is interesting to note that EPR-monitored redox titration experiments performed on purified ForCE1 buffered at pH 6.0 and 7.5 have provided values of E_m (MK/MKH₂) about 55 mV lower than that of the menaquinone pool. Such a shift can be explained by a ~ 80-fold tighter binding of oxidized MK than MKH₂ to the ForCE1 Q-site, which would be expected for a quinone reduction site in which binding of the substrate (menaquinone) is favored over that of the product (menaquinol). This situation is very similar to that described for the plastosemiquinone bound to the quinone reduction site QB in photosystem II ($\Delta = -50$ mV) (53). In addition, similar values have been measured for the demethylmenasemiquinone stabilized at the quinol oxidation site of the membrane-bound nitrate reductase from *E. coli* ($\Delta = -30$ or -80 mV) (54), and tighter binding of ubiquinol than ubiquinone has been discussed in the quinone reduction site of the *bc*₁ complex from yeast ($\Delta \sim +24$ to $+54$ mV) (55) or from *Rhodobacter sphaeroides* ($\Delta \sim +60$ mV) (56).

Within the enzymatic complex, the ForE1 subunit could help to stabilize menaquinone binding by providing a structural interface with ForC1 as in its absence the amount of copurified MK-7 drops dramatically to 1.6%. Moreover, ForE1 may participate to the structural integrity of ForC1 as its formate:benzyl viologen oxidoreductase activity dropped by 50 fold when produced and purified in absence of ForE1. Using several techniques, we have shown that MK-7 copurified with ForCE1 in a molar ratio (1:0.87). As discussed above, ForCE enzymes are not predicted to contain any transmembrane helices and are purified without detergents. Nevertheless, they bind menadione with an apparent affinity ($K_M^{\text{menadione}} = 20$ μM) in the same range as the membrane integral nitrate reductase A from *E. coli* and the peripheral type-II NADH:quinone oxidoreductase from *Caldalkalibacillus thermarum* (57, 58). Lastly, ForCE1 is also able to bind MK-8 at a low but significant ratio, consistent with low MK-8 abundance in *B. subtilis* membrane (48). To recruit menaquinone, it is reasonable to assume that ForCE contacts the membrane. Even if ForCE1 and ForCE2 have been purified without detergents, they could loosely bind the cytoplasmic side of the membrane through amphipathic helices similarly to the peripheral NdhH from *C. thermarum* that couples NADH oxidation to menaquinone reduction (59). Evaluation of this hypothesis is the object of undergoing studies in our laboratory.

ForC1 and ForC2 from *B. subtilis* are distinct from other members of the FDH family notably because of the residues at vicinity of the Mo atom such as the natural substitution of the strictly conserved His residue adjacent to Cys or Secys (C/UH) by a Gln (C/UQ) (Fig. 1A and S2A). This change from a positively charged and polar amino acid (His) by a polar one (Gln) is intriguing and prompted us to examine the active site region by sequence alignment and examination of the 3D-structures of FDHs (Fig. S7). This scrutinous analysis allowed us to pinpoint an His residue located beside of the strictly conserved Arg active residue and whose function may be to preserve at least one positive charge in close proximity to the active site (Fig. S7A). Furthermore, this analysis sheds light into the systematic occurrence of at least one His residue close to the active site with the occurrence of either a Gln residue (Class I: C/UH RGQ or C/UQ RGH as in ForC, Fig. S7A, B and

C), a Glu residue (Class II: C/UH RGE, Fig. S7D and E) or an His residue (Class III: C/UH RGH, Fig. S7F and G). As mentioned before, the importance of these residues and their mechanistic role at the active site are still unknown and this will be investigated in detail in forthcoming studies.

Phylogenetic analysis indicates that the ForC proteins of *B. subtilis* are the first characterized representatives of a new subfamily of FDHs with a CQ RGH motif. Indeed, using the ForC1 sequence as bait, 377 sequences with an N-terminal extension allowing the coordination of 4 [Fe-S] clusters were identified. These sequences belong to the previously mentioned classes I and III. Strikingly, the 176 sequences with the CQ RGH catalytic motif (Fig. S2A sequences shown in blue) cluster distinctly from the 201 sequences with the CH RGQ/H catalytic motif (Fig. S2A sequences shown in grey). The 176 sequences are mainly found in *Firmicutes* but some representatives are found in other bacterial phyla (*Proteobacteria*, *Actinobacteria*, *Deinococcus*, *Acidobacteria* and *Planctomycetes*) or in Archaea (Fig. S2B). Furthermore, the vast majority of sequences with the CQ RGH motif are synteny encoded with a gene encoding a protein with a DUF1641 domain, presumably a homolog of ForE.

While the *forC1* and *forC2* genes are paralogous and proteins have 61 % of identity, ForE1 and ForE2 share weak sequence identity (20%). However, both enzymatic complexes achieve the same reaction with comparable kinetic behavior and most likely interact loosely with the membrane to recruit menaquinone. A notable difference between both complexes resides in the way the corresponding operons are regulated. While genes encoding FDHs are typically regulated by anaerobiosis, fermentation and formate induction (60, 61), *forCE1* and *forCE2* do not seem expressed under these metabolic conditions (24, 28) and are upregulated by different environmental and cellular cues. Notably, the *forCE1* operon is part of the SigB-dependent general stress regulon and is upregulated in swarming conditions, in the presence of high salt or ethanol concentrations (28, 62, 63). On the other hand, the *forCE2* transcription is upregulated after germination and in exponential growth, and downregulated by the ResED two-component system that activate genes in oxygen limited conditions (28, 64).

Altogether, our results highlight the originality of these non-canonical FDHs, expand our knowledge on the FDHs' building blocks and pave the way for developing new biocatalysts for CO₂ reduction.

Experimental Procedures

Bacterial strains, media, and culture conditions

B. subtilis 168 (*trpC2*) strain and derivatives are described in Table S6. Genomic integration of reporter sequences was achieved using the pSPH1/pSPH2 plasmids (obtained by Dr Henrik Strahl von Schulten) by transformation at the *amyE* locus (65). Target integration was confirmed by amylase sensitivity. Chromosomal inactivation of target genes was obtained by transformation of genomic DNA (gDNA) from knock out strains (source BGSC, 64). Clones were verified by PCR. For routine growth, cells were propagated in LB medium (Tryptone, 10 g/L, Yeast Extract, 5 g/L, NaCl, 5 g/L). When necessary, antibiotics were used at the following concentrations: spectinomycin ($100 \mu\text{g mL}^{-1}$), kanamycin ($10 \mu\text{g mL}^{-1}$), and erythromycin ($1.25 \mu\text{g mL}^{-1}$).

For overproduction of recombinant proteins *B. subtilis* 168 derivatives (4088 *amyE*::pSHP1-6his*yjgCD*, 4233 *amyE*::pSHP2-*yjgC8his*, 4230 *amyE*::pSHP-6his*yrhED*, 4192 *amyE*::pSHP-*yrhE8his*) were grown in 4.8 L of LB medium with 2 μM sodium molybdate at 37°C until OD 0.3, cells were then submitted to a salt shock (0.4 M NaCl) for 30 min, followed by induction with 0.8% xylose for 3 hours (4088 and 4233 strains) and expression overnight (4230 and 4192 strains) at 37°C. Harvested cells were washed once in 20 mM sodium phosphate pH 7.5 50 mM Na₂SO₄ and cells were kept at -80°C until use.

Plasmid construction

Genes were cloned into pSPH1 and pSPH2 to allow induction with xylose promoter at *amyE* locus. Plasmids were constructed as following: pET28HT-YjgCD: *yjgCD* fragment was amplified with primers 898-899 using *B. subtilis* gDNA as template and inserted by ligation into a previously excised pET28dHT-*gapR* at *NdeI-KpnI* sites to add a 6-his tag sequence followed by a TEV cleavage site at the in 5' end of *yjgC*.; pSPH1-6his*yjgCD*: 6his-*yjgCD* was amplified with primers 941-952 using pET28HT-YjgCD as template and introduced by ligation into pSHP1 at *AvrII-XhoI* sites; pSPH1-6his*yrhED*: *yrhED* was amplified with primers 967-968 using *B. subtilis* 168 gDNA as template and introduced into pSPH1 at *AvrII-EcoRI* sites using Gibson Assembly® Cloning kit NEB with the linker primer 966. Cloning of *yrhE* at this site adds a sequence encoding a 6-his tag followed by a TEV cleavage site at 5' end. pSPH2-*yjgC8his*: *yjgC* was amplified with primers 944-950 and introduced into pSPH2 at *XhoI-SpeI* sites. Cloning of *yjgC* at this site adds a sequence encoding an 8-his tag at the 3' end; pSPH1-*yrhE8his*: pSPH2-*yjgC8his* was digested at *XhoI-SfiI* sites to release *yjgC* fragment. Then a *yrhE* fragment amplified with primers 988-1042 using *B. subtilis* gDNA as template and introduced by ligation.

All plasmids were verified by sequencing and primers are listed in Table S7

Protein purification

All steps were performed at 4°C with an Akta FPLC system (GE Healthcare). Frozen cells, typically 10-15 g of wet weight, were thawed, suspended in 90 mL of 20 mM sodium phosphate pH 7.5 50 mM Na₂SO₄ (buffer A). Cell suspension was treated with proteases inhibitor cocktail (Roche), lysozyme (1 mg/mL during 30 min at 37°C), DNase I and EDTA 0.5 mM and disrupted by

1-2 passages through a French pressure cell at 1 bar. Cells debris were removed by centrifugation for 40 min at 100,000 x g. The supernatant was applied onto 15 mL Ni-NTA affinity column (GE healthcare). Column was washed with buffer A supplemented with 50 mM imidazole and the enzyme eluted in buffer A supplemented with 500 mM imidazole and 10 mM KNO₃. Enzyme was washed in 50 mM MES pH 6, 50 mM Na₂SO₄, 5% glycerol and 10 mM KNO₃ using a PD-10 desalting column (Pharmacia), concentrated with Amicon 100 kDa (Millipore) and frozen in liquid nitrogen.

Activity Assays and Kinetic Analysis

FDH activity was determined using an Avaspec-2048L spectrophotometer, inside an anaerobic chamber, with an atmosphere of 100% N₂, at room temperature, with stirring. For formate:benzyl viologen (BV) oxidoreduction measurements, the reduction of BV was monitored at 600 nm ($\epsilon_{600\text{ nm}}(\text{BV}^+) = 7.0945\text{ mM}^{-1}\text{ cm}^{-1}$) with 1.75 mM BV in 25 mM CHES pH 8.6 (6his-YrhED) or 17.5 mM BV in 25 mM CHES pH 10 (YjgC-8his/ 6his-YjgCD) supplemented with 50 mM sodium formate at room temperature. One unit of activity is defined as the amount of FDH capable of oxidizing 1 μmol of formate per min per mg of enzyme. Kinetic analysis was measured at substrate concentrations ranging from 0.5 μM to 150 mM sodium formate. For formate:menadione oxidoreduction measurements, the reduction of 60 μM menadione was monitored at 260 nm ($\epsilon_{260\text{ nm}}(\text{Menadione}) = 17.2\text{ mM}^{-1}\text{ cm}^{-1}$) in 25 mM CHES pH 9 and 50 mM sodium formate at room temperature. One unit of activity is defined as the amount of FDH capable of reducing 1 μmol of menadione per min per mg of enzyme. Kinetic analysis was measured at substrate concentrations ranging from 0.5 μM to 200 μM menadione. Kinetic parameters were calculated by direct fitting of the Michaelis-Menten equation: $y = V_{\text{max}} \times S / (K_M + S)$ using Origin pro. The influence of pH on FDH activity was assessed using a buffer mix containing 20 mM MES, CHAPS, CHES, HEPES at room temperature. The pH was adjusted from 6.5 to 11 with HCl and NaOH.

Quinone extraction and analysis

Quinones were extracted from solutions of purified ForCE1, ForCE2 or ForC1 essentially as described (67). Briefly, 20-50 μL of purified proteins (corresponding to 0.1-0.25 mg protein) were transferred into glass tubes and completed up to 200 μL with water. 50 μL KCl 3 M and 3 mL methanol were added, and the tubes were vortexed for 1 min. 2 mL petroleum ether (40-60° boiling range) was added and vortex was repeated for 1 min. The tubes were centrifuged at 700 rpm for 1 min at room temperature, the upper phase was collected, and the methanol phase was extracted again with 2 mL petroleum ether. Both petroleum ether phases were combined in 5 mL eppendorf tubes and dried under a nitrogen flow. Dried lipid extracts were resuspended in 100 μL ethanol and fractions corresponding to 5 and 20 μg protein were analyzed by HPLC coupled to electrochemical detection (ECD) and mass spectrometry as previously described (68). The probe temperature was 400°C, the cone voltage was 80 V, and MS spectra were recorded between m/z 500 and 900 with a scan time of 0.5 s.

Commercial MK-7 (Sigma) was used to generate standard curves ranging from 2 to 100 pmoles. The concentration of the MK-7 solution was determined

using an extinction coefficient $\epsilon_{248\text{ nm}} = 18900\text{ M}^{-1}\text{ cm}^{-1}$ (69). The standard curve for the ECD signal was used to quantify the peaks (MK-7 and MK-8) obtained for the protein samples. Technical duplicates (extraction and analysis) were performed for each protein preparation and the quantifications of MKs represent the average of the four values obtained from two measurements (5 and 20 μg protein) for each duplicate.

Redox titrations.

Preparation of EPR samples.

Formate reduced samples of ForCE1 were prepared in 50 mM MES buffer pH 6.0 with 80 μM of protein as followed. The air-oxidized sample was incubated with 100 mM sodium formate in a glove box and frozen immediately. Subsequently, the sample was thawed in the glove box and further reduced with 13 mM sodium dithionite before freezing. Formate reduced samples of ForCE2 were prepared in 20 mM Tris/Propane pH 6.5 and 5% glycerol containing 50 μM of protein as followed. The air-oxidized sample was incubated with 30 mM sodium formate in a glove box before freezing, or incubated with 5 mM sodium dithionite in a glove box before freezing.

Redox titrations of the MSK radical in ForCE1 were carried out anaerobically at room temperature (about 25 °C) either in a glovebox or in an airtight vessel flushed with oxygen-free argon. Redox potentials were measured with a combined Pt-Ag/AgCl/KCl (3M) microelectrode and are given in the text with respect to the standard hydrogen electrode. The following redox mediators were used at 10 μM final concentrations: phenazine methosulfate, phenazine ethosulfate, methylene blue, resorufin, indigo carmin, anthraquinone 2,6 disulfate, flavin mononucleotide, phenosafranine, neutral red, methyl viologen. Reductive titrations were carried out by stepwise addition of an anaerobic sodium dithionite solution (100 mM or 1 mM). Samples were anaerobically transferred into calibrated EPR tubes that were rapidly frozen.

The normalized variation of the peak-to-peak amplitude of the menasemiquinone EPR signal was fitted to a theoretical curve corresponding to two successive one-electron redox processes:

$$A_{\text{ptp}} = \frac{1}{1 + e^{\alpha(E - E_1)} + e^{\alpha(E_2 - E)}} \quad (\text{Eq. 1})$$

where E_1 and E_2 are the midpoint potentials of the MK/MSK and MSK/MKH₂ couples, respectively. $\alpha = F/RT$ where R and F are the molar gas and Faraday constants, respectively, and T is the absolute temperature. The two-electron midpoint potential of the MK/MKH₂ couple, which corresponds to the redox potential for which the amount of MSK is maximum, is $E_m = (E_1 + E_2)/2$. The stability constant K_S of MSK defined with respect to the comproportionation reaction is

$$K_S = \frac{[\text{MSK}]^2}{[\text{MK}][\text{MKH}_2]} = e^{\alpha(E_1 - E_2)} \quad (\text{Eq. 2})$$

The occupancy level R_{occ} was calculated as the ratio between the normalized MSK concentration per enzyme inferred from spin quantitation experiments (assuming one [2Fe-2S] cluster taken as internal reference per enzyme), and the normalized maximal MSK concentration (MSK_{max}) given by

$$\text{MSK}_{\text{max}} = \frac{1}{1 + 2e^{\alpha/2 \times (E_2 - E_1)}} \quad (\text{Eq. 3})$$

Differences in the binding constants of MK (K_{MK}) and MKH₂ (K_{MKH_2}) manifest as a shift in the E_m from that of free MK/MKH₂ given by

$$E_m(\text{bound}) - E_m(\text{free}) = \frac{1}{2} \alpha \times \ln\left(\frac{K_{\text{MKH}_2}}{K_{\text{MK}}}\right) \quad (\text{Eq. 4})$$

The affinity of the site for MSK is a determinant of E_1 and E_2 but not of E_m .

Multifrequency EPR spectroscopy.

X- and Q-band EPR spectra were measured on a Bruker Eleksys E500 spectrometer. For X-band measurements, the spectrometer was equipped with an ER4012ST rectangular cavity fitted to an Oxford Instruments ESR900 helium flow cryostat. For Q-band measurements, a standard resonator equipped with an Oxford Instruments CF 935 cryostat was used. W-Band experiments were performed on a Bruker Eleksys E680 spectrometer equipped with a 6 T superconducting magnet and a 2 kG high resolution sweep coil. Spectra were recorded with the standard W-band resonator fitted with a Bruker cryogen-free system (Stinger). For the echo-detected field swept experiment, the two pulses echo intensity was measured as a function of magnetic field at fixed time interval $\tau = 200$ ns between the two microwave pulses, using a shot repetition time of 500 μs .

A field correction was applied to the magnetic field by simulating the overlapping spectral contribution of Mn²⁺, assuming $g(\text{Mn}^{2+}) = 2.00101 \pm 0.00005$ and an isotropic hyperfine coupling constant $a(\text{Mn}^{2+}) = -(8.710 \pm 0.003)$ mT (70).

Spectral simulations.

Numerical simulations of EPR spectra were performed with the EasySpin package (release 5.0.12) using Matlab (The MathWorks, Inc., US) (71). A field-independent (unresolved hyperfine couplings, H-strain) linewidth model was used to simulate the EPR signal of the menaemiquinone and of the Mo(V) species, whereas those of the FeS centers were simulated using a field-dependent (g-strain) linewidth model. For H-strain, the full width at half-maximum of Gaussian lines along the g-tensor principal axes were adjusted whereas the corresponding g-strains distributions were considered uncorrelated. Parameters used for the simulations shown in this work are provided in Table S8.

Mass spectrometry analysis

Purified proteins were subjected to an SDS-PAGE and the stacking gel band corresponding to total proteins was excised and submitted to in-gel trypsin digestion for proteomic analysis as described previously (72) and with the following adapted modifications. Spectra were processed by Proteome Discoverer software (ThermoFisher, version 2.4.1.15) using the Sequest HT algorithm with the *Bacillus subtilis* database (Taxonomy ID: 224308 version 2016-08-20, downloaded from NCBI by Protein Center including 5,573 entries). In this study, proteins were also filtered by a minimum number of

Peptide Spectral Match of 10. The list of identified proteins is available in Tables S2-4.

Data Availability

The mass spectrometry proteomics data have been deposited to the ProteomeXchange Consortium (<http://proteomecentral.proteomexchange.org>) via the PRIDE partner repository (73) with the dataset identifier PXD028742 and 10.6019/PXD028742.

Reviewer account details:

Username: reviewer_pxd028742@ebi.ac.uk

Password: 43qZRKSy

Acknowledgements and Funding

We thank Romain Mercier for providing plasmids pSPH1/pSPH2, originally constructed by H. Strahl von Schulten. We also thank Matt Cabeen, Elodie Foulquier-Khadaroo and Anne Galinier for providing protocols and advice for *B. subtilis* genetics and culture. We thank Anne Galinier and Frédéric Biaso for scientific discussions. We also thank Genevieve Shirley Dobihal and David Rudner for providing genomic DNA *Bacillus subtilis* 168 *trpC2 ΔyjdD::ery*, strain was originally constructed by (66). Marseille Protéomique (MaP) has been supported by IBiSA (Infrastructures en Biologie Santé et Agronomie) and Aix Marseille Université. The authors are grateful to the EPR facilities available at the French EPR network (RENARD, IR CNRS 3443) and the Aix-Marseille EPR center. This work was supported by the French National Research Agency (ANR MOLYERE project, Grant No. 16-CE29-0010-01), the CNRS and the CNRS Energy unit (Cellule Energie) through the project MICROBIOCO2. A. U. and M. B. were supported by a MESR fellowship and R.A-C by an ANR MOLYERE project post-doctoral fellowship.

Authors contribution

A.W., R.A-C. and S.G. designed experiments. A.U., A.W., F.P., F.S., G.G., M.B., R.A-C, R.L. and S.G. performed experiments. A.M., A.W., B.G, R.A.C. and S.G., wrote, reviewed & edited manuscript. A.M., B.G. and S.G. provided resources and obtained funding.

The authors declare that they have no conflicts of interest with the contents of this article.

References

1. Niks, D., and Hille, R. (2019) Molybdenum- and tungsten-containing formate dehydrogenases and formylmethanofuran dehydrogenases: Structure, mechanism, and cofactor insertion. *Protein Sci.* 28, 111–122
2. Schoepp-Cothenet, B., van Lis, R., Philippot, P., Magalon, A., Russell, M. J., and Nitschke, W. (2012) The ineluctable requirement for the trans-iron elements molybdenum and/or tungsten in the origin of life. *Sci. Rep.* 2, 263
3. Anbar, A. D. (2008) Elements and Evolution. *Science.* 322, 1481–1483
4. Catling, D. C., and Zahnle, K. J. (2020) The Archean atmosphere. *Sci. Adv.* 6, 9
5. Maia, L. B., Moura, I., and Moura, J. J. G. (2017) Molybdenum and tungsten-containing formate dehydrogenases: Aiming to inspire a catalyst for carbon dioxide utilization. *Inorganica Chim. Acta.* 455, 350–363
6. Nielsen, C. F., Lange, L., and Meyer, A. S. (2019) Classification and enzyme kinetics of formate dehydrogenases for biomanufacturing via CO₂ utilization. *Biotechnol. Adv.* 37, 107408
7. Magalon, A., Ceccaldi, P., and Schoepp-Cothenet, B. (2016) The Prokaryotic Mo/W-bisPGD Enzymes Family. *Molybdenum and Tungsten Enzymes*, 143–191
8. Hartmann, T., Schwanhold, N., and Leimkühler, S. (2015) Assembly and catalysis of molybdenum or tungsten-containing formate dehydrogenases from bacteria. *Biochim. Biophys. Acta BBA - Proteins Proteomics.* 1854, 1090–1100
9. Grimaldi, S., Schoepp-Cothenet, B., Ceccaldi, P., Guigliarelli, B., and Magalon, A. (2013) The prokaryotic Mo/W-bisPGD enzymes family: A catalytic workhorse in bioenergetic. *Biochim. Biophys. Acta BBA - Bioenerg.* 1827, 1048–1085
10. Arnoux, P., Ruppelt, C., Oudouhou, F., Lavergne, J., Siponen, M. I., Toci, R., Mendel, R. R., Bittner, F., Pignol, D., Magalon, A., and Walburger, A. (2015) Sulphur shuttling across a chaperone during molybdenum cofactor maturation. *Nat. Commun.* 6, 6148
11. Schrapers, P., Hartmann, T., Kositzki, R., Dau, H., Reschke, S., Schulzke, C., Leimkühler, S., and Haumann, M. (2015) Sulfido and Cysteine Ligation Changes at the Molybdenum Cofactor during Substrate Conversion by Formate Dehydrogenase (FDH) from *Rhodobacter capsulatus*. *Inorg. Chem.* 54, 3260–3271
12. Thomé, R., Gust, A., Toci, R., Mendel, R., Bittner, F., Magalon, A., and Walburger, A. (2012) A Sulfurtransferase Is Essential for Activity of Formate Dehydrogenases in *Escherichia coli*. *J. Biol. Chem.* 287, 4671–4678
13. Boyington, J. C., Gladyshev, V. N., Khangulov, S. V., Stadtman, T. C., and Sun, P. D. (1997) Crystal Structure of Formate Dehydrogenase H: Catalysis Involving Mo, Molybdopterin, Selenocysteine, and an Fe₄S₄ Cluster. *Science.* 275, 1305–1308
14. Maia, L. B., Moura, J. J. G., and Moura, I. (2015) Molybdenum and tungsten-dependent formate dehydrogenases. *J. Biol. Inorg. Chem.* 20, 287–309

15. Hartmann, T., Schrapers, P., Utesch, T., Nimtz, M., Rippers, Y., Dau, H., Mroginski, M. A., Haumann, M., and Leimkühler, S. (2016) The Molybdenum Active Site of Formate Dehydrogenase Is Capable of Catalyzing C–H Bond Cleavage and Oxygen Atom Transfer Reactions. *Biochemistry*. 55, 2381–2389
16. Popov, V. O., and Lamzin, V. S. (1994) NAD⁺-dependent formate dehydrogenase. *Biochem. J.* 301, 625–643
17. Yilmazer, B., Isupov, M. N., De Rose, S. A., Bulut, H., Benninghoff, J. C., Binay, B., and Littlechild, J. A. (2020) Structural insights into the NAD⁺-dependent formate dehydrogenase mechanism revealed from the NADH complex and the formate NAD⁺ ternary complex of the *Chaetomium thermophilum* enzyme. *J. Struct. Biol.* 212, 107657
18. Oliveira, A. R., Mota, C., Mourato, C., Domingos, R. M., Santos, M. F. A., Gesto, D., Guigliarelli, B., Santos-Silva, T., Romão, M. J., and Cardoso Pereira, I. A. (2020) Toward the Mechanistic Understanding of Enzymatic CO₂ Reduction. *ACS Catal.* 10, 3844–3856
19. Radon, C., Mittelstädt, G., Duffus, B. R., Bürger, J., Hartmann, T., Mielke, T., Teutloff, C., Leimkühler, S., and Wendler, P. (2020) Cryo-EM structures reveal intricate Fe-S cluster arrangement and charging in *Rhodobacter capsulatus* formate dehydrogenase. *Nat. Commun.* 11, 1912
20. Wagner, T., Ermler, U., and Shima, S. (2016) The methanogenic CO₂ reducing-and-fixing enzyme is bifunctional and contains 46 [4Fe-4S] clusters. *Science*. 354, 114–117
21. Jormakka, M., Törnroth, S., Byrne, B., and Iwata, S. (2002) Molecular basis of proton motive force generation: structure of formate dehydrogenase-N. *Science*. 295, 1863–1868
22. Hartmann, T., and Leimkühler, S. (2013) The oxygen-tolerant and NAD⁺-dependent formate dehydrogenase from *Rhodobacter capsulatus* is able to catalyze the reduction of CO₂ to formate. *FEBS J.* 280, 6083–6096
23. Oh, J. I., and Bowien, B. (1998) Structural analysis of the *fds* operon encoding the NAD⁺-linked formate dehydrogenase of *Ralstonia eutropha*. *J. Biol. Chem.* 273, 26349–26360
24. Glaser, P., Danchin, A., Kunst, F., Zuber, P., and Nakano, M. M. (1995) Identification and isolation of a gene required for nitrate assimilation and anaerobic growth of *Bacillus subtilis*. *J. Bacteriol.* 177, 1112–1115
25. Nakano, M. M., Dailly, Y. P., Zuber, P., and Clark, D. P. (1997) Characterization of anaerobic fermentative growth of *Bacillus subtilis*: identification of fermentation end products and genes required for growth. *J. Bacteriol.* 179, 6749–6755
26. Niks, D., Duvvuru, J., Escalona, M., and Hille, R. (2016) Spectroscopic and Kinetic Properties of the Molybdenum-containing, NAD⁺-dependent Formate Dehydrogenase from *Ralstonia eutropha*. *J. Biol. Chem.* 291, 1162–1174
27. Zuchan, K., Baymann, F., Baffert, C., Brugna, M., and Nitschke, W. (2021) The dyad of the Y-junction- and a flavin module unites diverse redox enzymes. *Biochim. Biophys. Acta Bioenerg.* 1862, 148401
28. Nicolas, P., Mäder, U., Dervyn, E., Rochat, T., Leduc, A., Pigeonneau, N., Bidnenko, E., Marchadier, E., Hoebeke, M., Aymerich, S., Becher, D., Bisicchia, P., Botella, E., Delumeau, O., Doherty, G., Denham, E. L.,

- Fogg, M. J., Fromion, V., Goelzer, A., Hansen, A., Härtig, E., Harwood, C. R., Homuth, G., Jarmer, H., Jules, M., Klipp, E., Chat, L. L., Lecoïnte, F., Lewis, P., Liebermeister, W., March, A., Mars, R. A. T., Nannapaneni, P., Noone, D., Pohl, S., Rinn, B., Rügheimer, F., Sappa, P. K., Samson, F., Schaffer, M., Schwikowski, B., Steil, L., Stülke, J., Wiegert, T., Devine, K. M., Wilkinson, A. J., Diji, J. M. van, Hecker, M., Völker, U., Bessières, P., and Noirot, P. (2012) Condition-Dependent Transcriptome Reveals High-Level Regulatory Architecture in *Bacillus subtilis*. *Science*. 335, 1103–1106
29. Zhu, B., and Stülke, J. (2018) SubtiWiki in 2018: from genes and proteins to functional network annotation of the model organism *Bacillus subtilis*. *Nucleic Acids Res.* 46, D743–D748
 30. Böhmer, N., Hartmann, T., and Leimkühler, S. (2014) The chaperone FdsC for *Rhodobacter capsulatus* formate dehydrogenase binds the bis-molybdopterin guanine dinucleotide cofactor. *FEBS Lett.* 588, 531–537
 31. Magalon, A., and Mendel, R. R. (2015) Biosynthesis and Insertion of the Molybdenum Cofactor. *EcoSal Plus.* 6, 2
 32. Axley, M. J., Grahame, D. A., and Stadtman, T. C. (1990) *Escherichia coli* formate-hydrogen lyase. Purification and properties of the selenium-dependent formate dehydrogenase component. *J. Biol. Chem.* 265, 18213–18218
 33. Schuchmann, K., and Müller, V. (2013) Direct and Reversible Hydrogenation of CO₂ to Formate by a Bacterial Carbon Dioxide Reductase. *Science*. 342, 1382–1385
 34. Grimaldi, S., Biaso, F., Burlat, B., and Guigliarelli, B. (2016) Electron Paramagnetic Resonance Studies of Molybdenum Enzymes. *Molybdenum and Tungsten Enzymes* 68–120
 35. Brondino, C. D., Passeggi, M. C. G., Caldeira, J., Almendra, M. J., Feio, M. J., Moura, J. J. G., and Moura, I. (2004) Incorporation of either molybdenum or tungsten into formate dehydrogenase from *Desulfovibrio alaskensis* NCIMB 13491; EPR assignment of the proximal iron-sulfur cluster to the pterin cofactor in formate dehydrogenases from sulfate-reducing bacteria. *J. Biol. Inorg. Chem.* 9, 145–151
 36. Biaso, F., Burlat, B., and Guigliarelli, B. (2012) DFT investigation of the molybdenum cofactor in periplasmic nitrate reductases: structure of the Mo(V) EPR-active species. *Inorg. Chem.* 51, 3409–3419
 37. Dermoun, Z., De Luca, G., Asso, M., Bertrand, P., Guerlesquin, F., and Guigliarelli, B. (2002) The NADP-reducing hydrogenase from *Desulfovibrio fructosovorans*: functional interaction between the C-terminal region of HndA and the N-terminal region of HndD subunits. *Biochim. Biophys. Acta.* 1556, 217–225
 38. Deaton, J. C., Solomon, E. I., Watt, G. D., Wetherbee, P. J., and Durfor, C. N. (1987) Electron paramagnetic resonance studies of the tungsten-containing formate dehydrogenase from *Clostridium thermoaceticum*. *Biochem. Biophys. Res. Commun.* 149, 424–430
 39. Jollie, D. R., and Lipscomb, J. D. (1991) Formate dehydrogenase from *Methylosinus trichosporium* OB3b. Purification and spectroscopic characterization of the cofactors. *J. Biol. Chem.* 266, 21853–21863
 40. Young, T., Nicks, D., Hakopian, S., Tam, T. K., Yu, X., Hille, R., and Blaha, G. M. (2020) Crystallographic and kinetic analyses of the FdsBG

- subcomplex of the cytosolic formate dehydrogenase FdsABG from *Cupriavidus necator*. *J. Biol. Chem.* 295, 6570–6585
41. Gardiner, A. T., Zech, S. G., MacMillan, F., Käss, H., Bittl, R., Schlodder, E., Lendzian, F., and Lubitz, W. (1999) Electron paramagnetic resonance studies of zinc-substituted reaction centers from *Rhodospseudomonas viridis*. *Biochemistry.* 38, 11773–11787
 42. Grimaldi, S., Lanciano, P., Bertrand, P., Blasco, F., and Guigliarelli, B. (2005) Evidence for an EPR-detectable semiquinone intermediate stabilized in the membrane-bound subunit NarI of nitrate reductase A (NarGHI) from *Escherichia coli*. *Biochemistry.* 44, 1300–1308
 43. Hastings, S. F., Kaysser, T. M., Jiang, F., Salerno, J. C., Gennis, R. B., and Ingledew, W. J. (1998) Identification of a stable semiquinone intermediate in the purified and membrane bound ubiquinol oxidase-cytochrome bd from *Escherichia coli*. *Eur. J. Biochem.* 255, 317–323
 44. Ingledew, W. J., Ohnishi, T., and Salerno, J. C. (1995) Studies on a stabilisation of ubisemiquinone by *Escherichia coli* quinol oxidase, cytochrome bo. *Eur. J. Biochem.* 227, 903–908
 45. Sato-Watanabe, M., Itoh, S., Mogi, T., Matsuura, K., Miyoshi, H., and Anraku, Y. (1995) Stabilization of a semiquinone radical at the high-affinity quinone-binding site (QH) of the *Escherichia coli* bo-type ubiquinol oxidase. *FEBS Lett.* 374, 265–269
 46. Lanciano, P., Magalon, A., Bertrand, P., Guigliarelli, B., and Grimaldi, S. (2007) High-stability semiquinone intermediate in nitrate reductase A (NarGHI) from *Escherichia coli* is located in a quinol oxidation site close to heme bD. *Biochemistry.* 46, 5323–5329
 47. Liebl, U., Pezennec, S., Riedel, A., Kellner, E., and Nitschke, W. (1992) The Rieske FeS center from the gram-positive bacterium PS3 and its interaction with the menaquinone pool studied by EPR. *J. Biol. Chem.* 267, 14068–14072
 48. Sato, T., Yamada, Y., Ohtani, Y., Mitsui, N., Murasawa, H., and Araki, S. (2001) Production of menaquinone (vitamin K₂)-7 by *Bacillus subtilis*. *J. Biosci. Bioeng.* 91, 16–20
 49. Un, S., Dorlet, P., and Rutherford, A. W. (2001) A high-field EPR tour of radicals in photosystems I and II. *Appl. Magn. Reson.* 21, 341–361
 50. Grimaldi, S., Ostermann, T., Weiden, N., Mogi, T., Miyoshi, H., Ludwig, B., Michel, H., Prisner, T. F., and MacMillan, F. (2003) Asymmetric binding of the high-affinity Q(H)^(*)(-) ubisemiquinone in quinol oxidase (bo3) from *Escherichia coli* studied by multifrequency electron paramagnetic resonance spectroscopy. *Biochemistry.* 42, 5632–5639
 51. Hille, R., Hall, J., and Basu, P. (2014) The Mononuclear Molybdenum Enzymes. *Chem. Rev.* 114, 3963–4038
 52. Page, C. C., Moser, C. C., Chen, X., and Dutton, P. L. (1999) Natural engineering principles of electron tunnelling in biological oxidation–reduction. *Nature.* 402, 47–52
 53. De Causmaecker, S., Douglass, J. S., Fantuzzi, A., Nitschke, W., and Rutherford, A. W. (2019) Energetics of the exchangeable quinone, QB, in Photosystem II. *Proc. Natl. Acad. Sci. U. S. A.* 116, 19458–19463
 54. Rendon, J., Pilet, E., Fahs, Z., Seduk, F., Sylvi, L., Hajj Chehade, M., Pierrel, F., Guigliarelli, B., Magalon, A., and Grimaldi, S. (2015) Demethylmenaquinol is a substrate of *Escherichia coli* nitrate reductase

- A (NarGHI) and forms a stable semiquinone intermediate at the NarGHI quinol oxidation site. *Biochim. Biophys. Acta.* 1847, 739–747
55. Covian, R., Zwicker, K., Rotsaert, F. A., and Trumpower, B. L. (2007) Asymmetric and redox-specific binding of quinone and quinol at center N of the dimeric yeast cytochrome bc₁ complex. Consequences for semiquinone stabilization. *J. Biol. Chem.* 282, 24198–24208
 56. Robertson, D. E., Prince, R. C., Bowyer, J. R., Matsuura, K., Dutton, P. L., and Ohnishi, T. (1984) Thermodynamic properties of the semiquinone and its binding site in the ubiquinol-cytochrome c (c₂) oxidoreductase of respiratory and photosynthetic systems. *J. Biol. Chem.* 259, 1758–1763
 57. Giordani, R., Buc, J., Cornish-Bowden, A., and Cárdenas, M. L. (1997) Kinetics of Membrane-Bound Nitrate Reductase A from *Escherichia Coli* with Analogues of Physiological Electron Donors. *Eur. J. Biochem.* 250, 567–577
 58. Blaza, J. N., Bridges, H. R., Aragão, D., Dunn, E. A., Heikal, A., Cook, G. M., Nakatani, Y., and Hirst, J. (2017) The mechanism of catalysis by type-II NADH:quinone oxidoreductases. *Sci. Rep.* 7, 40165
 59. Heikal, A., Nakatani, Y., Dunn, E., Weimar, M. R., Day, C. L., Baker, E. N., Lott, J. S., Sazanov, L. A., and Cook, G. M. (2014) Structure of the bacterial type II NADH dehydrogenase: a monotopic membrane protein with an essential role in energy generation. *Mol. Microbiol.* 91, 950–964
 60. Oh, J. I., and Bowien, B. (1999) Dual control by regulatory gene *fdsR* of the *fds* operon encoding the NAD⁺-linked formate dehydrogenase of *Ralstonia eutropha*. *Mol. Microbiol.* 34, 365–376
 61. Pinske, C., and Sawers, R. G. (2016) Anaerobic Formate and Hydrogen Metabolism. *EcoSal Plus.* 7, 1
 62. Höper, D., Völker, U., and Hecker, M. (2005) Comprehensive characterization of the contribution of individual SigB-dependent general stress genes to stress resistance of *Bacillus subtilis*. *J. Bacteriol.* 187, 2810–2826
 63. Petersohn, A., Brigulla, M., Haas, S., Hoheisel, J. D., Völker, U., and Hecker, M. (2001) Global Analysis of the General Stress Response of *Bacillus subtilis*. *J. Bacteriol.* 183, 5617–5631
 64. Ye, R. W., Tao, W., Bedzyk, L., Young, T., Chen, M., and Li, L. (2000) Global Gene Expression Profiles of *Bacillus subtilis* Grown under Anaerobic Conditions. *J. Bacteriol.* 182, 4458–4465
 65. Dubnau, D., and Davidoff-Abelson, R. (1971) Fate of transforming DNA following uptake by competent *Bacillus subtilis*. I. Formation and properties of the donor-recipient complex. *J. Mol. Biol.* 56, 209–221
 66. Koo, B.-M., Kritikos, G., Farelli, J. D., Todor, H., Tong, K., Kimsey, H., Wapinski, I., Galardini, M., Cabal, A., Peters, J. M., Hachmann, A.-B., Rudner, D. Z., Allen, K. N., Typas, A., and Gross, C. A. (2017) Construction and Analysis of Two Genome-Scale Deletion Libraries for *Bacillus subtilis*. *Cell Syst.* 4, 291-305
 67. Szyttenholm, J., Chaspoul, F., Bauzan, M., Ducluzeau, A.-L., Chehade, M. H., Pierrel, F., Denis, Y., Nitschke, W., and Schoepp-Cothenet, B. (2020) The controversy on the ancestral arsenite oxidizing enzyme; deducing evolutionary histories with phylogeny and thermodynamics. *Biochim. Biophys. Acta BBA - Bioenerg.* 1861, 148252

68. Pelosi, L., Vo, C.-D.-T., Abby, S. S., Loiseau, L., Rascalou, B., Hajj Chehade, M., Faivre, B., Goussé, M., Chenal, C., Touati, N., Binet, L., Cornu, D., Fyfe, C. D., Fontecave, M., Barras, F., Lombard, M., and Pierrel, F. (2019) Ubiquinone Biosynthesis over the Entire O₂ Range: Characterization of a Conserved O₂-Independent Pathway. *mBio*. 10 e01319-19
69. McMillan, D. G. G., Marritt, S. J., Butt, J. N., and Jeuken, L. J. C. (2012) Menaquinone-7 Is Specific Cofactor in Tetraheme Quinol Dehydrogenase CymA. *J. Biol. Chem.* 287, 14215–14225
70. Burghaus, O., Plato, M., Rohrer, M., Moebius, K., MacMillan, F., and Lubitz, W. (1993) 3-mm High-field EPR on semiquinone radical anions Q.^{•-} related to photosynthesis and on the primary donor P.^{•+} and acceptor QA.^{•-} in reaction centers of *Rhodobacter sphaeroides* R-26. *J. Phys. Chem.* 97, 7639–7647
71. Stoll, S., and Schweiger, A. (2006) EasySpin, a comprehensive software package for spectral simulation and analysis in EPR. *J. Magn. Reson.* 178, 42–55
72. Santin, Y. G., Doan, T., Lebrun, R., Espinosa, L., Journet, L., and Cascales, E. (2018) In vivo TssA proximity labelling during type VI secretion biogenesis reveals TagA as a protein that stops and holds the sheath. *Nat. Microbiol.* 3, 1304–1313
73. Perez-Riverol, Y., Csordas, A., Bai, J., Bernal-Llinares, M., Hewapathirana, S., Kundu, D. J., Inuganti, A., Griss, J., Mayer, G., Eisenacher, M., Pérez, E., Uszkoreit, J., Pfeuffer, J., Sachsenberg, T., Yilmaz, S., Tiwary, S., Cox, J., Audain, E., Walzer, M., Jarnuczak, A. F., Ternent, T., Brazma, A., and Vizcaíno, J. A. (2019) The PRIDE database and related tools and resources in 2019: improving support for quantification data. *Nucleic Acids Res.* 47, D442–D450
74. Yang, J., and Zhang, Y. (2015) I-TASSER server: new development for protein structure and function predictions. *Nucleic Acids Res.* 43, W174–W181
75. Gumerov, V. M., and Zhulin, I. B. (2020) TREND: a platform for exploring protein function in prokaryotes based on phylogenetic, domain architecture and gene neighborhood analyses. *Nucleic Acids Res.* 48, W72–W76
76. Letunic, I., and Bork, P. (2021) Interactive Tree Of Life (iTOL) v5: an online tool for phylogenetic tree display and annotation. *Nucleic Acids Res.* 49, W293–W296
77. George, G. N., Hilton, J., Temple, C., Prince, R. C., and Rajagopalan, K. V. (1999) Structure of the Molybdenum Site of Dimethyl Sulfoxide Reductase. *J. Am. Chem. Soc.* 121, 1256–1266
78. Jepson, B. J. N., Anderson, L. J., Rubio, L. M., Taylor, C. J., Butler, C. S., Flores, E., Herrero, A., Butt, J. N., and Richardson, D. J. (2004) Tuning a Nitrate Reductase for Function. *J. Biol. Chem.* 279, 32212–32218
79. Barber, M. J., May, H. D., and Ferry, J. G. (1986) Inactivation of Formate Dehydrogenase from *Methanobacterium formicicum* by Cyanide. *Biochemistry.* 25, 8150–8155
80. Jepson, B. J. N., Mohan, S., Clarke, T. A., Gates, A. J., Cole, J. A., Butler, C. S., Butt, J. N., Hemmings, A. M., and Richardson, D. J. (2007)

- Spectropotentiometric and Structural Analysis of the Periplasmic Nitrate Reductase from *Escherichia coli*. *J. Biol. Chem.* 282, 6425–6437
81. Najmudin, S., González, P. J., Trincão, J., Coelho, C., Mukhopadhyay, A., Cerqueira, N. M. F. S. A., Romão, C. C., Moura, I., Moura, J. J. G., Brondino, C. D., and Romão, M. J. (2008) Periplasmic nitrate reductase revisited: a sulfur atom completes the sixth coordination of the catalytic molybdenum. *J. Biol. Inorg. Chem.* 13, 737–753
 82. Gangeswaran, R., Lowe, D. J., and Eady, R. R. (1993) Purification and characterization of the assimilatory nitrate reductase of *Azotobacter vinelandii*. *Biochem. J.* 289, 335–342
 83. Butler, C. S., Charnock, J. M., Bennett, B., Sears, H. J., Reilly, A. J., Ferguson, S. J., Garner, C. D., Lowe, D. J., Thomson, A. J., Berks, B. C., and Richardson, D. J. (1999) Models for Molybdenum Coordination during the Catalytic Cycle of Periplasmic Nitrate Reductase from *Paracoccus denitrificans* Derived from EPR and EXAFS Spectroscopy. *Biochemistry.* 38, 9000–9012
 84. Dementin, S., Arnoux, P., Frangioni, B., Grosse, S., Léger, C., Burlat, B., Guigliarelli, B., Sabaty, M., and Pignol, D. (2007) Access to the Active Site of Periplasmic Nitrate Reductase: Insights from Site-Directed Mutagenesis and Zinc Inhibition Studies. *Biochemistry.* 46, 9713–9721
 85. Arnoux, P., Sabaty, M., Alric, J., Frangioni, B., Guigliarelli, B., Adriano, J.-M., and Pignol, D. (2003) Structural and redox plasticity in the heterodimeric periplasmic nitrate reductase. *Nat. Struct. Biol.* 10, 928–934
 86. Simpson, P. J. L., McKinzie, A. A., and Codd, R. (2010) Resolution of two native monomeric 90kDa nitrate reductase active proteins from *Shewanella gelidimarina* and the sequence of two *napA* genes. *Biochem. Biophys. Res. Commun.* 398, 13–18
 87. Butler, C. S., Charnock, J. M., Garner, C. D., Thomson, A. J., Ferguson, S. J., Berks, B. C., and Richardson, D. J. (2000) Thiocyanate binding to the molybdenum centre of the periplasmic nitrate reductase from *Paracoccus pantotrophus*. *Biochem J.* 352, 859–64.
 88. Rivas, M. G., González, P. J., Brondino, C. D., Moura, J. J. G., and Moura, I. (2007) EPR characterization of the molybdenum(V) forms of formate dehydrogenase from *Desulfovibrio desulfuricans* ATCC 27774 upon formate reduction. *J. Inorg. Biochem.* 101, 1617–1622
 89. Prisner, T., Lyubenova, S., Atabay, Y., MacMillan, F., Kröger, A., and Klimmek, O. (2003) Multifrequency cw-EPR investigation of the catalytic molybdenum cofactor of polysulfide reductase from *Wolinella succinogenes*. *J. Biol. Inorg. Chem.* 8, 419–426

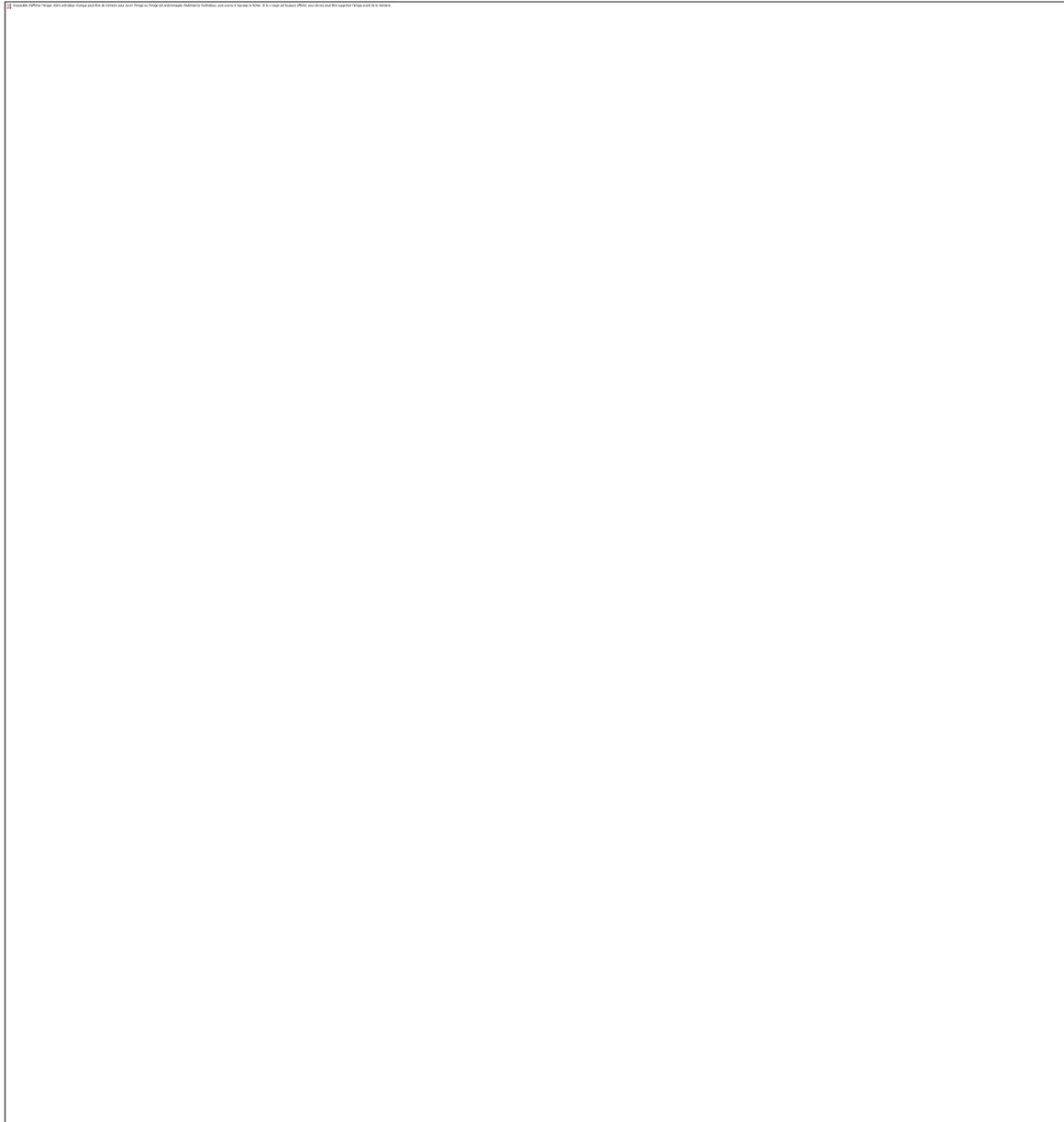


Figure 1. *B. subtilis* genome encodes putative non-canonical FDHs

A. Alignment of the amino acids involved in the active site of characterized FDH enzymes and of the two putative FDH proteins from *B. subtilis* (red asterisks). Consensus sequence (blue box) shows which amino acids are conserved with a 50% threshold. FDHs have been organized into 3 classes according to the sequence and organization of their active site (Fig. S7): Class I: C/UH RGQ or C/UQ RGH, Class II: C/UH RGE and Class III: C/UH RGH. Overview of the full sequence alignment is shown in Fig. S1B.

B. Genomic organization of *yjgCD* (ForCE1) and *yrhED* (ForCE2) in *B. subtilis*.

C. Structural model of YjgC generated with i-tasser (74) using FdsA from *R. capsulatus* (PDB ID: 6TGA). FeS clusters are named according to their proximity to the Mo cofactor in the 3D-structural model.

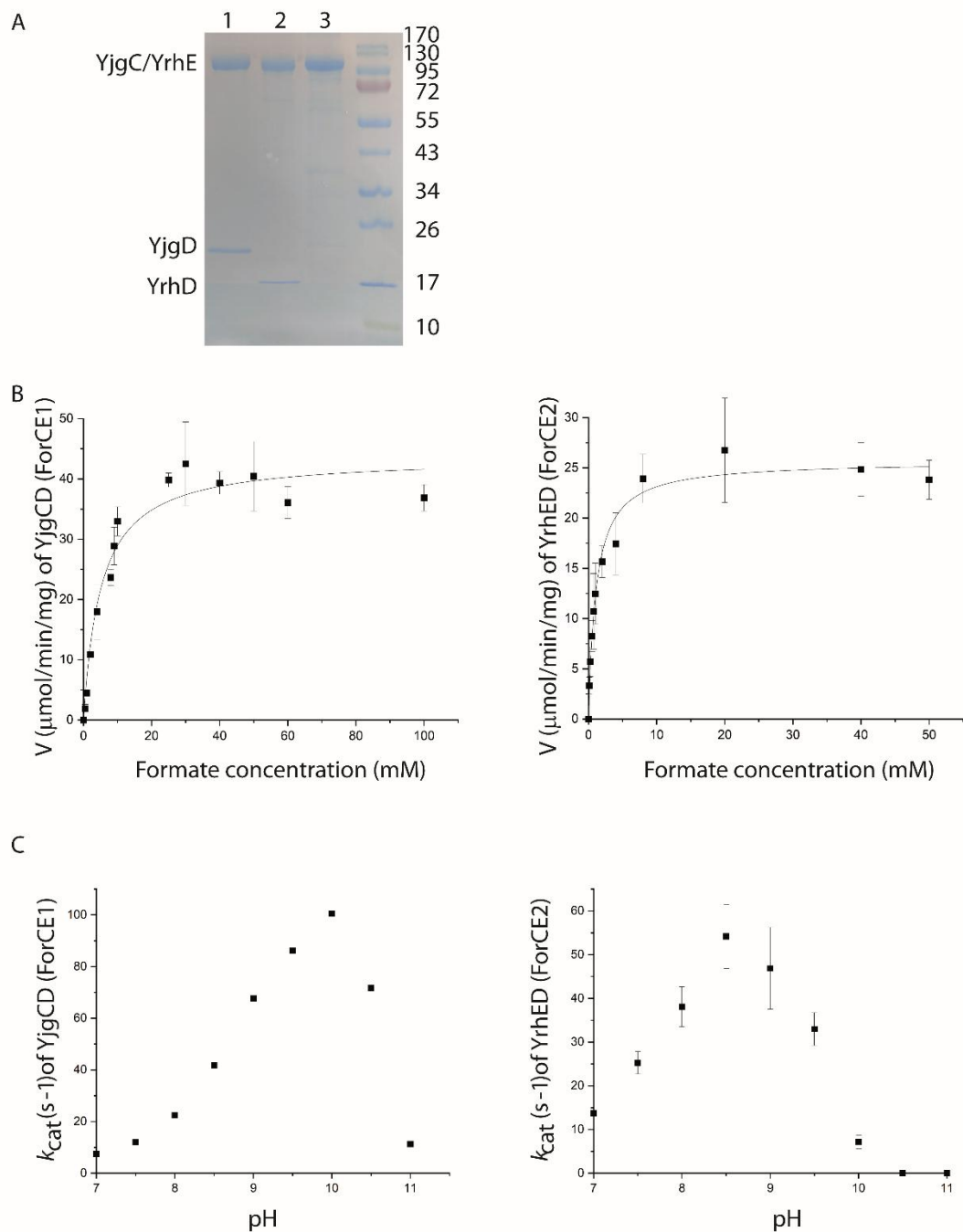


Figure 2: YjgCD (ForCE1) and YrhED (ForCE2) are formate-oxidizing enzymes

A: Purified proteins are analyzed on Coomassie Brilliant Blue-stained 15% SDS-polyacrylamide gel. Molecular standards are indicated in kDa. Lane 1: YjgC N-terminus 6his-tagged copurifies with YjgD; Lane 2 YrhE N-terminus 6his-tagged copurifies with YrhD; Lane 3: YjgC C-terminus 8his-tagged was purified without YjgD.

B: Michaelis-Menten plot for the formate:benzyl viologen oxidoreductase reaction of YjgCD (ForCE1) at pH 10 and YrhED (ForCE2) at pH 8.6.

C: pH dependence of k_{cat} (s^{-1}) for YjgCD (ForCE1) and YrhED (ForCE2).

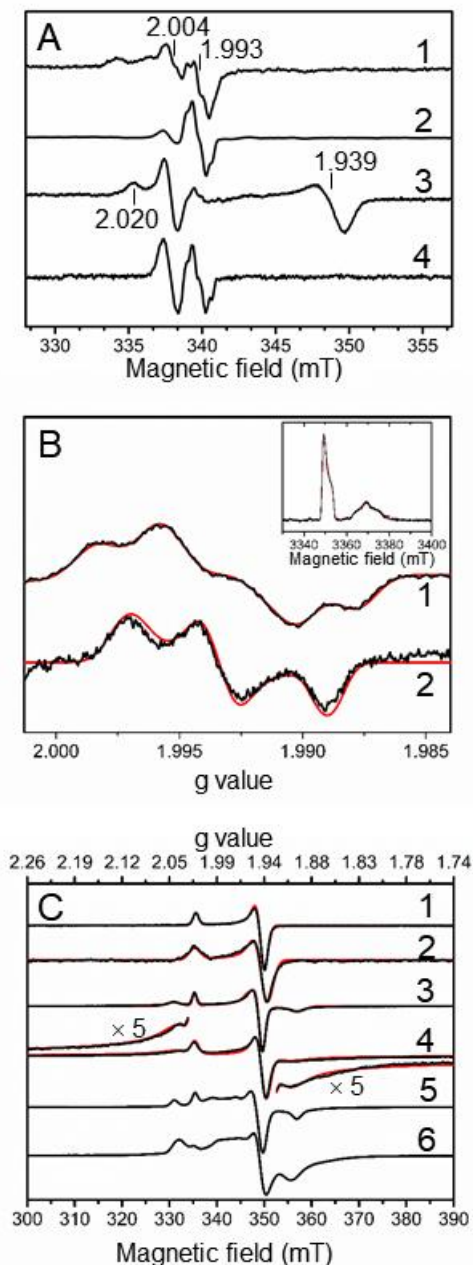


Figure 3. EPR characterization of the cofactors in ForCE1 and ForCE2.

A. Air-oxidized (1,2) and formate-reduced (3,4) ForCE1 (1,3) and ForCE2 (2,4) collected at 50 K (1) or 70 K (2-4). Other experimental conditions: microwave power, 4 mW, field modulation amplitude, 0.4 mT (1,2) or 0.2 mT (3,4) at 100 kHz, microwave frequency, ~ 9.48 GHz. Vertical lines indicate remarkable g values given in the figure and discussed in the main text.

B. Continuous wave Mo(V) EPR spectra in air-oxidized ForCE2 samples measured at X-band (9.47864 GHz) (1) and Q-band (34.1187 GHz) (2) frequencies. Other experimental conditions: temperature, 70 K (1) and 50 K (2), microwave power, 1 mW (1) and 0.1 mW (2), field modulation amplitude, 0.1 mT (1) and 0.5 mT (2) at 100 kHz. The inset shows the echo-detected field swept EPR spectrum measured at 50 K at W-band (94.0014 GHz) frequency. Other experimental conditions: microwave pulse lengths, 20 ns and 40 ns for $\pi/2$ and π pulses, respectively.

C. EPR spectra of dithionite-reduced ForCE1 (1,3,5) and ForCE2 (2,4,6) measured at 100 K (1,2), 50 K (3,4) or 15 K (5,6). Other experimental conditions: microwave power, 1 mW (1) or 10 mW (2-6), modulation amplitude 1 mT (1-2, 4-6) or 0.4 mT (3) at 100 kHz, microwave frequency, ~ 9.48 GHz. Spectral simulations are displayed as red traces superimposed to the experimental spectra and have been performed using the parameters given in the main text and in the Supplementary Information (Table S8).

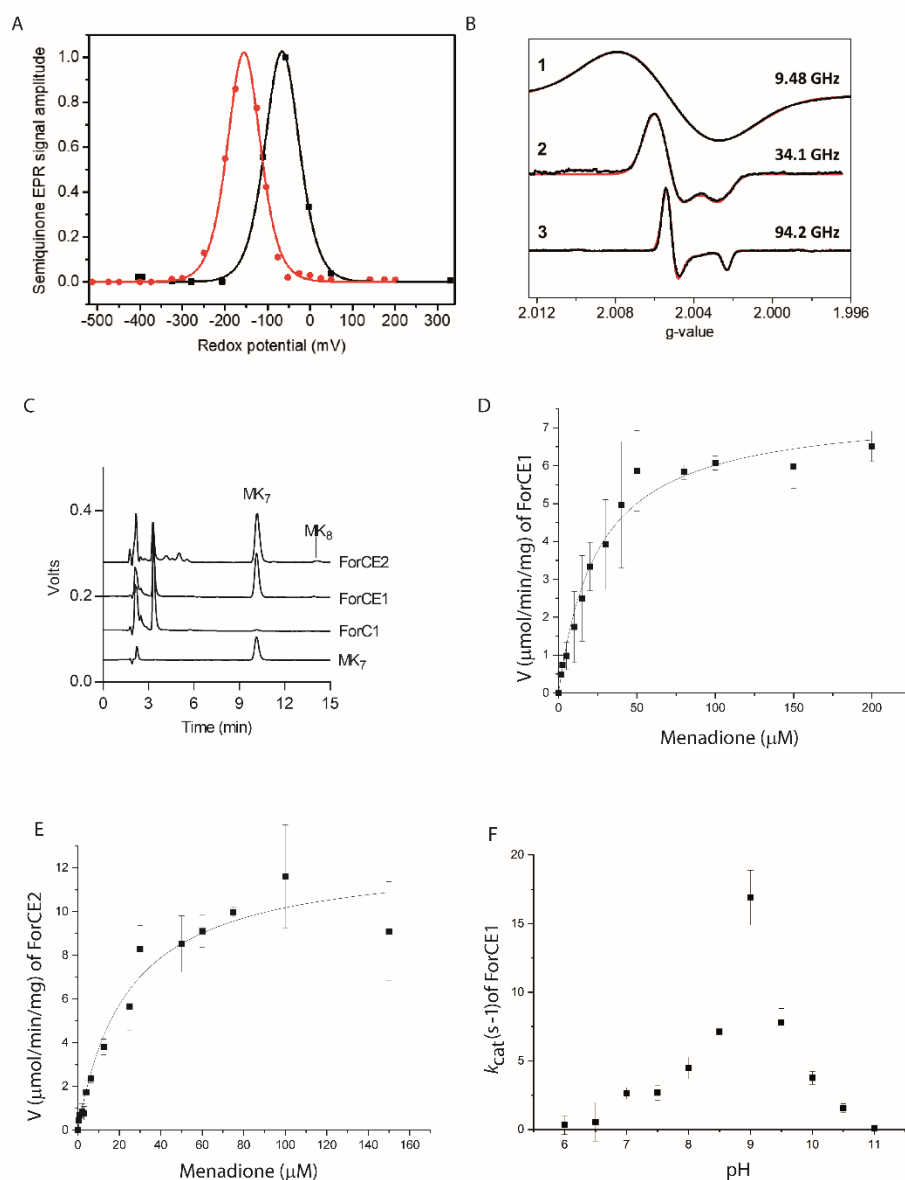


Figure 4. ForCE1 and ForCE2 bind MK-7 as an electron sink

A. Normalized redox titration curves of the MSK radical in ForCE1 buffered at pH = 6 (black) or 7.5 (red). Experimental points (filled squares or filled circles) have been fitted to the theoretical curve as described in the experimental procedures section. Experimental conditions: temperature, 50 K, microwave power, 10 mW, modulation amplitude, 0.5 mT (pH 7.5) or 1 mT (pH 6) at 100 kHz.

B. g-scale representation of the cw EPR spectra (black traces) and their simulation (red traces) of the MSK radical in ForCE1 buffered at pH = 6 and measured at X-band (9.4812 GHz) (1), Q-band (34.094 GHz) (2) and W-band (94.244 GHz) (3). Spectra were simulated using the same rhombic g-tensor with principal values $g_{1,2,3} = 2.0054, 2.0051, \text{ and } 2.0023$ and the linewidths given in the supplementary information (Table S8). Experimental conditions: temperature, 50 K, microwave power, 4 mW (1), 0.1 mW (2) or 0.05 mW (3), field modulation amplitude at 100 kHz, 0.4 mT (1, 3) or 0.5 mT (2).

- C. ForCE1 and ForCE2, but not ForC1, bind large quantities of MK-7. HPLC-ECD analysis of the MK-7 standard (15 pmol) and of lipid extracts corresponding to ~ 40 pmol of purified proteins.
- D. Michaelis-Menten plot for the formate:menadione oxidoreduction reaction of ForCE1 at pH 9
- E. Michaelis-Menten plot for the formate:menadione oxidoreduction reaction of ForCE2 at pH 9
- F. pH dependence of k_{cat} (s^{-1}) for ForCE1.

FDH	K_M^{formate} (mM)	k_{cat} (s^{-1})	V_{max} (U)	pH
YjgCD/ForCE1	$5.1 \pm 0,9$	96.1 ± 4	43.7 ± 1.9	10
YrhED/ForCE2	1.1 ± 0.1	55.8 ± 1.6	26.6 ± 0.8	8.6
YjgC/ForC1	ND	2.13 ± 0.05	1.16 ± 0.03	10
	$K_M^{\text{menadione}}$ (mM)	k_{cat} (s^{-1})	V_{max} (U)	pH
YjgCD/ForCE1	0.025 ± 0.003	16.5 ± 0.6	7.5 ± 0.3	9
YrhED/ForCE2	0.023 ± 0.005	26.4 ± 1.8	12.6 ± 0.9	9
YjgC/ForC1	ND	0	0	9

Table 1: Enzymatic catalytic constants for Formate oxidation by YjgCD, YjgC and YrhED using either benzyl viologen (top) or menadione (bottom) as electron acceptors.

Supporting information

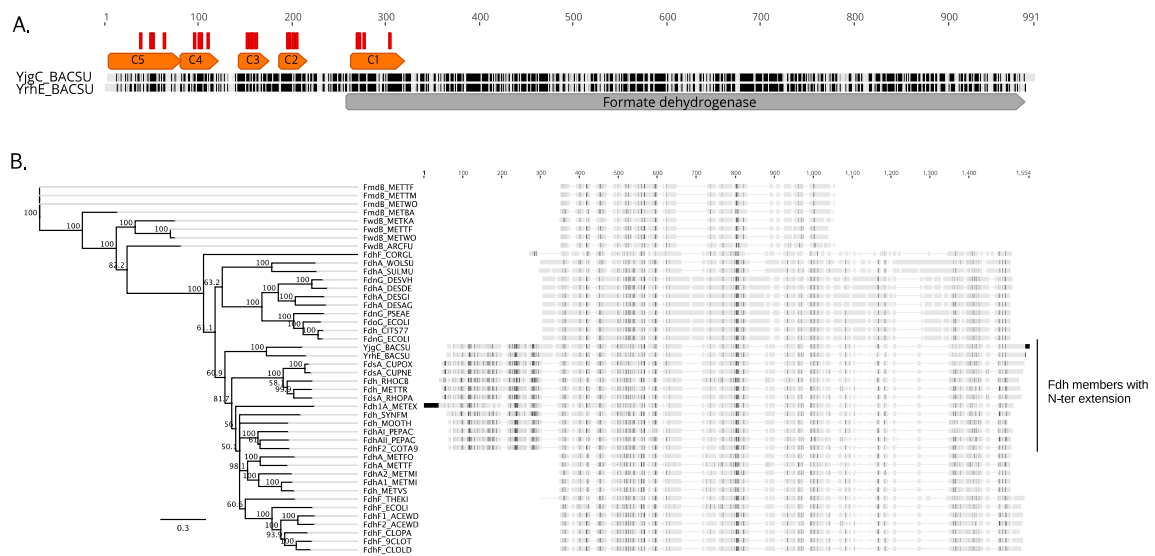


Figure S1. Phylogenetic tree and alignment of catalytic subunits of characterized Mo/W-bisPGD-containing FDH enzymes.

A. Pairwise sequence alignment of YjgC and YrhE from *B. subtilis* with predicted regions for [Fe-S] clusters C1 to C5 (orange) and Mo/W-bisPGD cofactor binding motif (grey). Position of amino acids involved in iron coordination are highlighted in red. Conserved amino acids between sequences are black-colored.

B. Full sequence alignment of 42 characterized FDH enzymes and of the two putative FDH proteins from *B. subtilis*. Alignments generated with Geneious Prime® 2020.1.1 (Global alignment: blosum62 matrix, Gap open penalty 12, Gap ext penalty 3 and 1000 refinement iterations, Tree building: Jukes-Cantor genetic distance model, neighbor joining method, no outgroup with resampling bootstrap and 1000 replicates). Protein sequences description is detailed in Table S1.

Figure S2. Distribution of ForC and related proteins with the CQ RGH and CH RGQ/H motif.

A. Phylogenetic tree of 377 sequences related to ForC and FdsA proteins and distribution of the CQ RGH and CH RGQ/H motif. The sequence dataset was obtained by merging the results of 3 independent BLAST searches, using the ForC1 sequence from *B. subtilis* as bait for the first search and the sequence with the lowest similarity score but displaying the CQ-RGH motif as a query for the other two consecutive searches. The results of each BLAST search were analysed with TREND (75) to remove sequence redundancy (CD-HIT: 0.9) and sequences lacking an N-terminal extension allowing coordination of 4 [Fe-S] clusters were removed. The final batch of sequences (377) was aligned and FdsA from *C. necator* was used as the root for phylogenetic tree construction. Sequences with a CQ RGH motif are colored in blue while the other are colored in grey.

B. Phylogenetic and taxonomy distribution of 176 sequences with the CQ RGH motif and the FsdA sequence from *C. necator*. The presence of a ForE (DUF1641) homolog in synteny with the ForC related protein was determined with TREND or by manual search. ForC1 and ForC2 from *B. subtilis* are highlighted in red, FsdA from *C. necator* is highlighted in black.

Alignments and phylogenetic trees were generated with Geneious Prime® 2020.1.1 (Global alignment: blosum62 matrix, Gap open penalty 12, Gap ext penalty 3 and 1000 refinement iterations, Tree building: Jukes-Cantor genetic distance model, neighbor joining method, outgroup FsdA from *C. necator* (WP_011614623) with resampling bootstrap and 1000 replicates). Phylogenetic tree in Fig S2A was edited using iTOL (76). The 377 sequence identifiers used for the phylogenetic tree are found in the Supplementary Information Table S9.

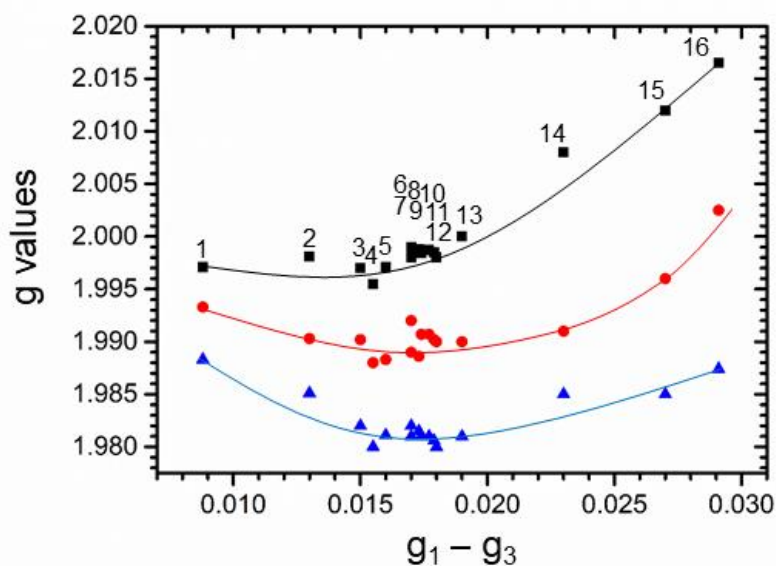


Figure S3: Plot of the g values of Mo(V) species against g -tensor anisotropy for selected bacterial and eukaryotic Mo/W-*bis*PGD enzymes with Cys or SeCys ligand. g_1 , g_2 and g_3 values are indicated by black squares, red circles and blue triangles, respectively. Nonlinear correlations can be extrapolated and are schematically indicated by solid lines. Data sets correspond to 1: *Bacillus subtilis* ForCE2 (this work), 2: *R. sphaeroides* dimethylsulfoxide reductase (S147C variant) (77), 3: *Synechococcus* sp. PCC 7942 assimilatory nitrate reductase NarB (78), 4: *Methanobacterium formicicum* FDH incubated with potassium cyanide (79), 5: *E. coli* periplasmic nitrate reductase NapA (80), 6: *Desulfovibrio desulfuricans* NapA (high g turnover Mo(V) species) (81), 7: *Azotobacter vinelandii* assimilatory nitrate reductase NAS (82), 8: *Paracoccus denitrificans* NapAB (83), 9: *R. sphaeroides* NapA (84), 10: *R. sphaeroides* NapAB (85), 11: *Shewanella gelidimarina* NapA (86), 12: *Paracoccus pantotrophus* NapAB (83), 13: *D. desulfuricans* NapA (high g nitrate Mo(V) species) (81), 14: *Paracoccus pantotrophus* NapAB incubated with thiocyanate (87), 15: *Desulfovibrio desulfuricans* FDH (88), 16: *Wolinella succinogenes* polysulfite reductase (89).

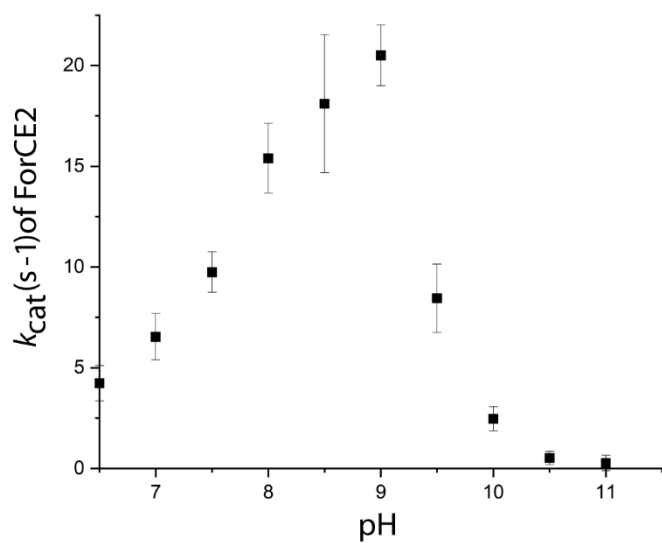
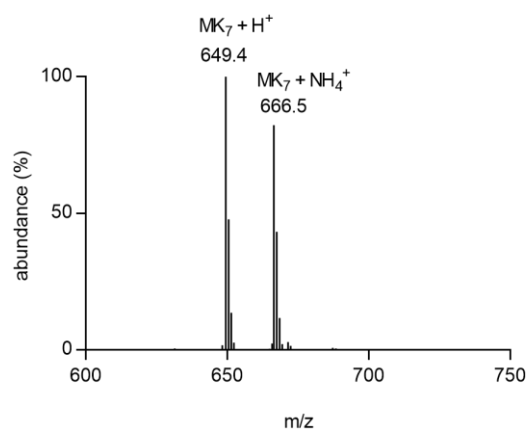
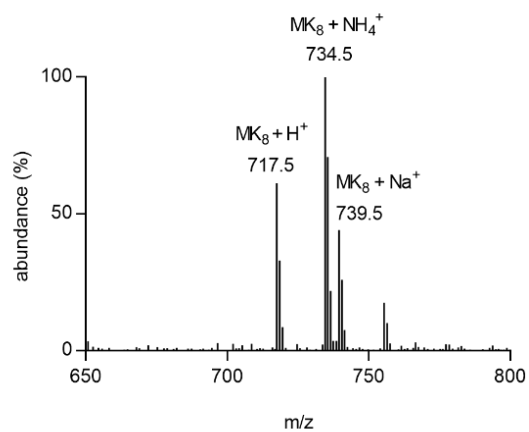


Figure S4: pH dependence of k_{cat} (s^{-1}) for formate:menadione oxidoreduction by ForCE2.

A**B****Figure S5: Mass spectra of MK-7 and MK-8 by HPLC-MS**

A: Mass spectrum of MK-7 (eluting at 11.5 min) obtained by HPLC-MS analysis of lipid extracted from purified ForCE1.

B: Mass spectrum of MK-8 (eluting at 13.95 min) obtained by HPLC-MS analysis of lipid extracted from purified ForCE1.

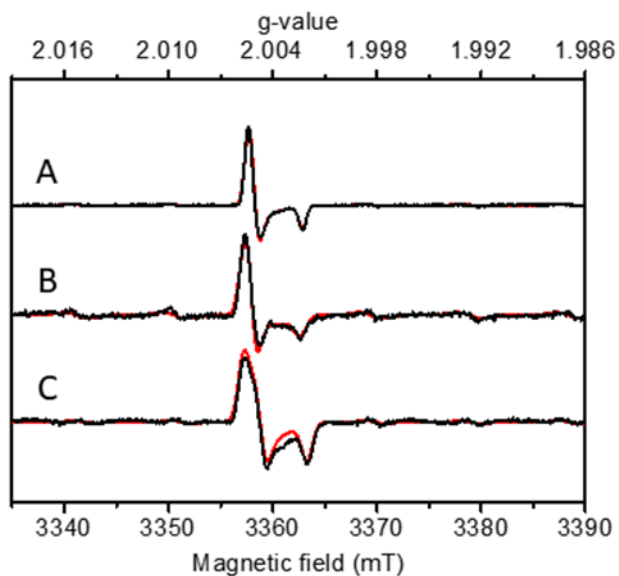


Figure S6: W-band cw EPR spectra of MSK stabilized in ForCE1 (A), ForCE2 (B) and EcNarGHI (C). Simulations are shown in red and are superimposed to the experimental spectra shown in black. Simulation parameters are: g-tensor principal values $g_{1,2,3} = 2.0054, 2.0051, 2.0023$ (A), $2.0056, 2.0051, 2.0023$ (B), $2.0058, 2.0048, 2.0022$ (C). H-strain parameters (25.8, 25.8, 24.2) MHz (A), (33.6, 27.2, 38.1) MHz (B) and (34.4, 36.5, 34.2) MHz. (C). Experimental conditions: temperature, 50 K, microwave power, 0.05 mW (A, B) and 0.005 mW (C), modulation amplitude, 0.4 mT at 100 kHz (A, B) or at 10 kHz (C), microwave frequency, 94.2441 GHz (A), 94.0012 GHz (B) and 94.2493 GHz (C).

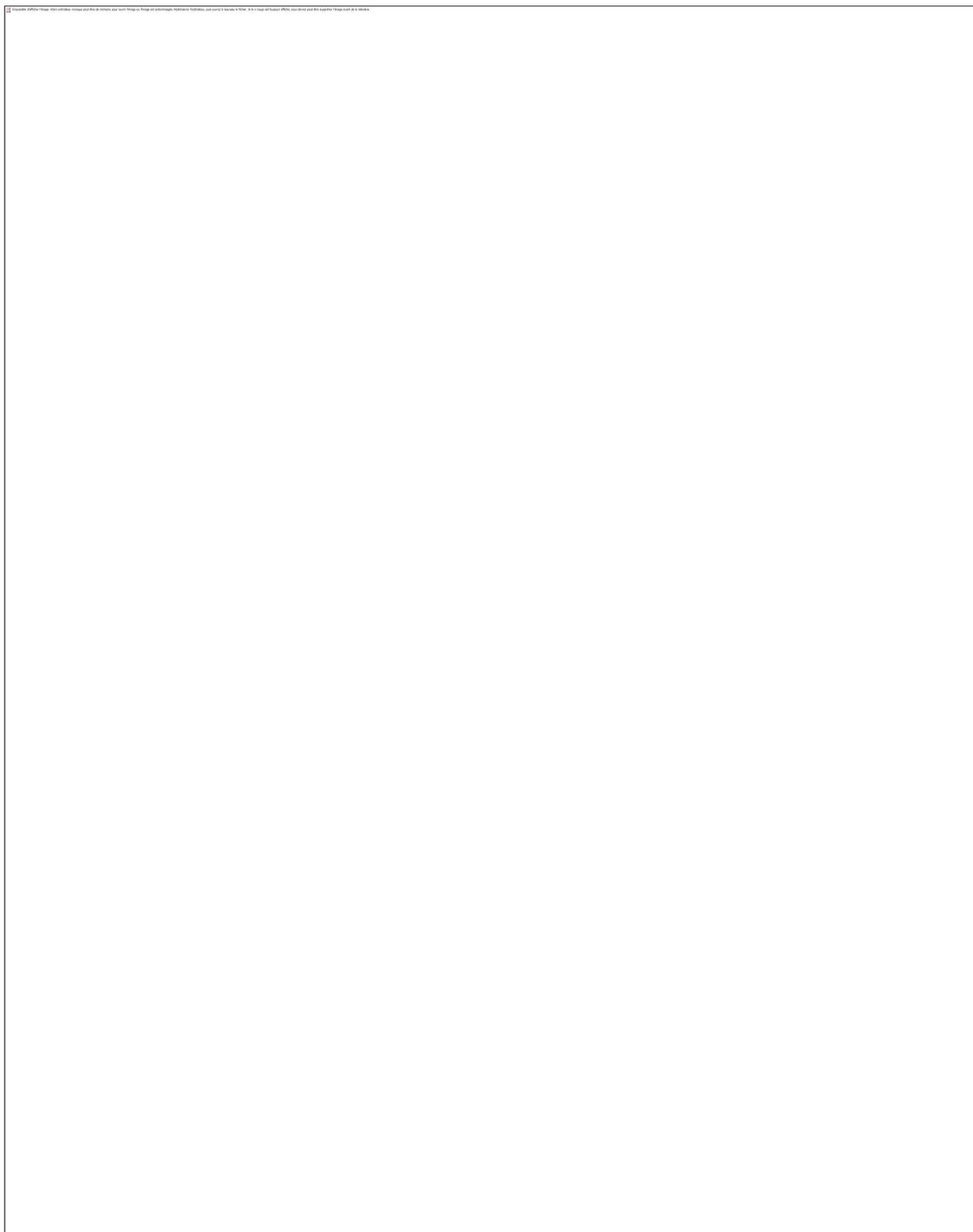


Figure S7. Amino acids surrounding the Mo/W atom in FDHs active site and their classification. Mo/W (blue), ligands (yellow and white), *bis*-PGD (pink) and amino acids (cyan)

Class I type C/UH-RGQ: A. ForC1 model with CQ-RGH (based on 6TGA structure), B. FdsA from *R. capsulatus* (pdb: 6TGA) and C. FdhF from *E. coli* (pdb:1FDO)

Class II type UH-RGE: D. FdhA from *D. gigas* (pdb:1H0H) and E. FdhA from *D. vulgaris* (pdb: 6SDR)

Class III type UH-RGH: F. FwdBD from *M. wolfeii* (pdb: 5T5i) and G. FdnG from *E. coli* (pdb:1KQF).

Table S1: FDH sequences used for alignments in figures 1A and S1B.

Protein Name	Organism	Identifier
FmdB_METTF	<i>Methanothermobacter thermautotrophicus</i>	P95295
FmdB_METTM	<i>Methanothermobacter marburgensis</i>	D9PXE7
FmdB_METWO	<i>Methanothermobacter wolfeii</i>	O74033
FmdB_METBA	<i>Methanosarcina barkeri</i>	Q48945
FwdB_METKA	<i>Methanopyrus kandleri</i>	Q8TYN5
FwdB_METTF	<i>Methanothermobacter thermautotrophicus</i>	Q59580
FwdB_METWO	<i>Methanothermobacter wolfeii</i>	O74032
FwdB_ARCFU	<i>Archaeoglobus fulgidus</i>	O28350
FdhF_CORGL	<i>Corynebacterium glutamicum</i>	Q8NSY6
FdhA_WOLSU	<i>Wolinella succinogenes</i>	Q7M971
FdhA_SULMU	<i>Sulfurospirillum multivorans</i>	Q6W8A3
FdnG_DESVH	<i>Desulfovibrio vulgaris</i>	Q727P3
FdhA_DESDE	<i>Desulfovibrio desulfuricans</i>	Q1KRL6
FdhA_DESGI	<i>Desulfovibrio gigas</i>	Q934F5
FdhA_DESAG	<i>Desulfovibrio alaskensis</i>	Q314X8
FdhG_PSEAE	<i>Pseudomonas aeruginosa</i>	Q14T72
FdoG_ECOLI	<i>Escherichia coli (strain K12)</i>	P32176
Fdh_CITS77	<i>Citrobacter sp. S77</i>	WP_136345514
FdnG_ECOLI	<i>Escherichia coli (strain K12)</i>	P24183
YjgC_BACSU	<i>Bacillus subtilis (strain 168)</i>	O34720
YrhE_BACSU	<i>Bacillus subtilis (strain 168)</i>	Q795Y4
FdsA_CUPOX	<i>Cupriavidus oxalaticus</i>	A0A4P7LDP8
FdsA_CUPNE	<i>Cupriavidus necator</i>	O87815
Fdh_RHOBC	<i>Rhodobacter capsulatus</i>	D5AQH0
Fdh_METTR	<i>Methylosinus trichosporium OB3b</i>	A0A2D2D2X1
FdsA_RHOPA	<i>Rhodopseudomonas palustris</i>	Q6NBU4
Fdh1A_METEX	<i>Methylobacterium extorquens</i>	Q8KTI7
Fdh_SYNFM	<i>Syntrophobacter fumaroxidans</i>	A0LP28
Fdh_MOOTH	<i>FdhA Moorella thermoacetica</i>	P77908
FdhAII_PEPAC	<i>Peptoclostridium acidaminophilum</i>	Q93V05
FdhAI_PEPAC	<i>Peptoclostridium acidaminophilum</i>	Q93V06
FdhF2_GOTA9	<i>Gottschalkia acidurici</i>	K0B3A3
FdhA_METFO	<i>Methanobacterium formicicum</i>	P06131
FdhA_METTF	<i>Methanothermobacter thermautotrophicus</i>	Q50569
FdhA2_METMI	<i>Methanococcus maripaludis</i>	Q877E3
FdhA1_METMI	<i>Methanococcus maripaludis</i>	Q877E4
Fdh_METVS	<i>Methanococcus vanniellii</i>	A6UPU2
FdhF_THEKI	<i>Thermoanaerobacter kivui</i>	A0A097ATK5
FdhF_ECOLI	<i>Escherichia coli</i>	P07658
FdhF1_ACEWD	<i>Acetobacterium woodii</i>	H6LB59
FdhF2_ACEWD	<i>Acetobacterium woodii</i>	H6LB61
FdhF_CLOPA	<i>Clostridium pasteurianum</i>	A0A0H3IZZ5
FdhF_9CLOT	<i>Clostridium carboxidivorans P7</i>	C6PQ41
FdhF_CLOLD	<i>Clostridium ljungdahlii</i>	D8GPQ2

Table heading for Tables S2-4: NCBI accession number; Protein name, name in NCBI; % of Coverage, percent protein sequence coverage by the matching peptides; Peptide Spectral Match, number of peptide spectral matches given by the Sequest algorithm corresponding to the total number of identified peptide sequences for the protein, including those redundantly identified; Unique peptides, number of distinct peptides matching to protein sequence and unique to this protein; MW (kDa), theoretical molecular mass of the identified protein (given by Sequest algorithm).

Table S2: Mass spectrometry analysis of His-YjgCD/ForCE1 purification

Table S3: Mass spectrometry analysis of YjgC-His/ForC1 purification

Table S4: Mass spectrometry analysis of His-YrhED/ForCE2 purification

Table S5: HPLC-ECD quantification of MK in lipid extracts of purified ForCE1, ForCE2 and ForC1 (n=2 independent purifications)

FDH	MK-7 (pmol/pmol of protein)	MK-8 (pmol/pmol of protein)
ForCE1	0.87 ± 0.092	0.025 ± 0.009
ForC1	0.016 ± 0.001	ND
ForCE2	1.63 ± 0.82	0.035 ± 0.009

Table S6: Strains used in this work

Strains	Description	Reference
4161	<i>Bacillus subtilis</i> 168 <i>trpC2</i>	BGSC
4088	<i>Bacillus subtilis</i> 168 <i>trpC2 amyE::pSHP1-6his yjgCD</i>	This work
4089	<i>Bacillus subtilis</i> 168 <i>trpC2 amyE::pSHP2-yjgC8his</i>	This work
4040	<i>Bacillus subtilis</i> 168 <i>trpC2 ΔyjgD::ery</i>	This work, (58)
4233	<i>Bacillus subtilis</i> 168 <i>trpC2 ΔyjgD::ery amyE::pSHP2-yjgC8his</i>	This work
4156	<i>Bacillus subtilis</i> 168 <i>trpC2 ΔyjgC::kan</i>	BGSC
4167	<i>Bacillus subtilis</i> 168 <i>trpC2 ΔresE::ery</i>	BGSC
4191	<i>Bacillus subtilis</i> 168 <i>trpC2 ΔresE::ery amyE::pSHP1-6his yrhED</i>	This work
4192	<i>Bacillus subtilis</i> 168 <i>trpC2 ΔresE::ery amyE::pSHP2-yrhE8his</i>	This work
4230	<i>Bacillus subtilis</i> 168 <i>trpC2 ΔresE::ery ΔyjgC::kan amyE::pSHP1-6his yrhED</i>	This work

Table S7: Primers used in this work

Primer	Sequence (5' to 3')
898	atttgatattccaaggtcatatggctggcaagaaaacaatcaca
899	tcgagtgcggccgcaagctcaatctcgcttattcattcctt
941	atgcatctagaaaggagattcctaggatggctcaccaccaccaccac
944	gatgggtaccgggccccccctcgagatggctggcaagaaaacaatcac
952	caagctatcgataccgtcgacctcgagtcaatctcgcttattcattcc
966	atgacataaaatgcatctagaaaggagattcctaggatggctcaccaccaccaccaccacgaaaat ttgtattccaaggtcatatgatg
967	cgaaaatttgatattccaaggtcatatgatggacgtaagtcgatcagtg
968	cgcgccgctctagaactagaattcttattgttctcgaagttctttccc
988	gatgggtaccgggccccccctcgagatgatggacgtaagtcgatcagtg
1042	ggtggtggtggtggtggccattatggccatcagtcagatgtacatagccag

Table S8. Parameters used to simulate the EPR spectra shown in this work.

EPR-active species	Enzyme	Magnetic parameters	Linewidth parameters	Microwave frequency band
Mo(V)	ForCE2	$g_{1,2,3} = 1.9971, 1.9934, 1.9890$ $A_{1,2,3} = 12.5, 12.4 \text{ \& } 11.0 \text{ MHz}$	9.7, 12.0 & 8.9 MHz	X
			25.8, 20.7 & 19.4 MHz	Q
			82.7, 68.5 & 76.7 MHz	W
MSK	ForCE1	$g_{1,2,3} = 2.0054, 2.0051, 2.0023$	28.5, 25.5 & 26.9 MHz	X
			25.8, 25.8 & 24.2 MHz	Q
			22.2, 28.4 & 21.1 MHz	W
$[2\text{Fe-2S}]^{1+}$	ForCE1	$g_{12}, g_3 = 2.0180, 1.9373$	0.0085, 0.0116	X
$[2\text{Fe-2S}]^{1+}$	ForCE2	$g_{12}, g_3 = 2.0203, 1.9357$	0.0164, 0.0176	X
$[4\text{Fe-4S}]^{1+}$	ForCE1	$g_{1,2,3} = 2.0474, 1.9484, 1.8966$	0.0227, 0.0117, 0.0194	X
$[4\text{Fe-4S}]^{1+}$	ForCE2	$g_{1,2,3} = 2.0295, 1.9401, 1.9119$	0.0328, 0.6009, 0.0170	X

¹ with colinear g- and proton hyperfine tensors

Table S9: FDH identifiers used for the phylogenetic tree in Figure S2